Correspondence to:

B. Campforts,
benjamin.campforts@colorado.edu

The Art of Landslides: How Stochastic Mass Wasting Shapes Topography and Influences Landscape Dynamics

Benjamin Campforts[1], Charles M. Shobe[2], Irina Overeem[1,3], and Gregory E. Tucker[3,4]

[1]Institute of Arctic and Alpine Research, University of Colorado Boulder, Boulder, CO, USA, [2]Department of Geology and Geography, West Virginia University, Morgantown, WV, USA, [3]Department of Geological Sciences, University of Colorado Boulder, Boulder, CO, USA, [4]Cooperative Institute for Research in Environmental Sciences (CIRES), University of Colorado Boulder, Boulder, CO, USA

Abstract Bedrock landslides shape topography and mobilize large volumes of sediment. Yet, interactions between landslide-produced sediment and fluvial systems that together govern large-scale landscape evolution are not well understood. To explain morphological patterns observed in steep, landslide-prone terrain, we explicitly model stochastic landsliding and associated sediment dynamics. The model accounts for several common landscape features such as slope frequency distributions, which include values in excess of regional stability limits, quasi-planar hillslopes decorated with straight, closely spaced channel-like features, and accumulation of sediment in valley networks rather than on hillslopes. Stochastic landsliding strongly affects the magnitude and timing of sediment supply to the fluvial system. We show that intermittent sediment supply is ultimately reflected in topography. At dynamic equilibrium, landslide-derived sediment pulses generate persistent landscape dynamism through the formation and breaching of landslide dams and epigenetic gorges as landslides force shifts in channel positions. Our work highlights the importance of interactions between landslides and sediment dynamics that ultimately control landscape-scale response to environmental change.

Plain Language Summary Landslides are natural hazards that predominantly occur where geologic forces have created steep, rugged terrain. Yet from a geologic perspective, landsliding is also one of the forces that contributes to shaping the landscape. Gaining insight into the role of landslides in shaping topography is critical to better understand the interplay between the factors driving long-term landscape evolution, and ultimately controlling landslide hazard. Here, we use a computer simulation model to study how landslides help shape terrain. Simulating landslides enables us to identify the origins of several common features in mountainous topography. Model results illustrate how repeated landsliding can cause rivers and ridgelines to gradually but continually shift position over time, such that some mountain drainages grow while others shrink. This type of computer model, which describes how topography and landsliding influence one another, can help the scientific community understand the response of steep terrain to environmental changes, such as those related to climate and earthquakes.

1. Introduction

Bedrock landslides are highly efficient geomorphic agents (Broeckx et al., 2020; Eisbacher & Clague, 1984; Hovius et al., 1997; Korup et al., 2007; Larsen & Montgomery, 2012; Ouimet et al., 2007). Landslides can produce sediment at rates that exceed the maximum rate of sediment generation by weathering processes (Dixon & von Blanckenburg, 2012), and can trigger a chain of processes that alter the pathways of sediment from source to sink (Fan et al., 2019). The continuously growing data realm of remotely sensed Earth observations and analytical measurements such as cosmogenic radionuclide (CRN) derived erosion rates helps to better understand the impact of mass movements on evolving surfaces (e.g., DeLisle et al., 2022; Depicker et al., 2021). Yet, quantifying the impact of landslides on the evolution of landscapes over large spatial and temporal scales requires computational models that explicitly simulate sediment production, mobilization, and aggradation.

Although topographic relief is a necessary condition for—and a dominant control on—landslide susceptibility (Pourghasemi et al., 2018), process-based understanding of how landslides shape terrain is currently lacking. Over timescales relevant to the formation of topography, landslides, and other forms of mass wasting are thought to impose an upper limit to relief based on rock strength (Schmidt & Montgomery, 1995; Selby, 1982). Landsliding is often held to effectively impose a threshold slope angle on a landscape. Threshold theory implies that

an increased rate of fluvial incision, for example, due to accelerated rock uplift, would be accommodated by a commensurate increase in landslide frequency and/or magnitude without a notable change in hillslope angles (Burbank et al., 1996; Carson & Petley, 1970; Larsen & Montgomery, 2012; Montgomery, 2001; Tucker & Bras, 1998). While threshold-slope theory is consistent with an observed inverse correlation between drainage density and relief (Tucker & Bras, 1998; Tucker & Whipple, 2002), it does not account for several potentially important effects observed using remotely sensed and geochronologic data (Roering et al., 2015). For example, in its most idealized form, threshold slope theory implies a narrow frequency distribution of slope angles centered on a threshold angle for stability, which is at odds with the broader, symmetrical to right-skewed distributions that are commonly observed (Korup, 2008). Open questions remain about how the inherently episodic nature of landslides (Korup et al., 2004) influences fluvial sediment load and intermittent sediment aggradation (Croissant et al., 2017; Yanites et al., 2010), drainage network mobility (Dahlquist et al., 2018), and channel profile evolution through the formation of autogenic knickpoints and epigenetic gorges (Korup, 2006; Ouimet et al., 2008).

A disequilibrium exists between soil formation or weathering on the one hand and uplift rates or catchment wide denudation rates on the other. Based on the global compilation of Dixon and von Blanckenburg (2012), maximum soil production rates range between 0.12 and 0.17 mm yr^{-1} on average, with outliers up to 2 mm yr^{-1} (Larsen et al., 2014). These soil production rates are significantly lower than documented maximum catchment wide denudation rates ranging between 4 and 6 mm yr^{-1} (Harel et al., 2016; Portenga & Bierman, 2011). The difference between soil production/weathering and catchment wide denudation rates is often attributed to rapid erosion and mobilization of sediment through mass wasting (DiBiase et al., 2010; Dixon & von Blanckenburg, 2012). Yet, rapid sediment production mechanisms that could explain this offset are often disregarded when simulating landscape evolution. Commonly, soil thickness is predicted using an empirically validated soil production equation (A. M. Heimsath et al., 1997). Under dynamic equilibrium where rock uplift relative to baselevel (U) balances the weathering of bedrock or the production of soil, one obtains a steady weathered thickness (H, [L]) given by:

$$H = -H^* \ln \left(\frac{U}{P_0} \right)$$

(1)

where U represents the rock uplift rate [LT^{-1}], P_0 represents the maximum soil formation rate under zero soil thickness [LT^{-1}], and H^* is the soil production decay depth [L]. This formulation only yields physically realistic values (a positive soil thickness) as long as $P_0 \geq U$. Once U exceeds P_0, realistic soil thicknesses cannot be predicted any longer. This is in contrast with observations from regions where U exceeds the maximum soil production rate, such as the Himalayas (Lupker et al., 2012) or Taiwan (Fuller et al., 2006), where sediment is being produced faster than the apparent "speed limit" of soil production, resulting in high catchment-wide denudation rates (Dixon & von Blanckenburg, 2012; A. Heimsath et al., 2012). In order to explain sediment production and redistribution in catchments undergoing high uplift and erosion rates, landscape evolution models (LEM's) that explicitly simulate bedrock landslides and associated sediment production and transport are required.

Continuum geomorphic transport laws (Dietrich et al., 2003) predict landscapes that evolve toward a dynamic equilibrium in which erosion rates balance rock uplift rates (e.g., Whipple, 2001). Laboratory experiments and field observations indicate that landscape equilibrium is indeed a dynamic one, in which channels, valleys, and ridgelines may continue to shift and rearrange (Beeson et al., 2017; Hasbargen & Paola, 2000). Yet most LEMs predict equilibrium drainage networks that are fixed in space and time, unless some mechanism for lateral channel mobility is explicitly incorporated (e.g., Kwang et al., 2021; Langston & Tucker, 2018; Pelletier, 2004). One reason fluvial channels remain mobile in mountainous regions is that the debris from landslides can shift the position of a channel within its valley (Dahlquist et al., 2018). In addition, a landslide deposit can sometimes dam a valley entirely, leading to the formation of an aggradational zone upstream in which sediment deposition promotes lateral channel mobility (Croissant et al., 2017).

The goals of this paper are to evaluate (a) whether long term landslide activity can explain diagnostic features of the topography of landslide-prone regions, (b) how landslides contribute to the production and distribution of sediment over geological timescales, and (c) whether the interaction between landslides, sediment dynamics, and fluvial incision causes dynamism in the landscape that persists even when approaching an average equilibrium condition.

2. Models of Landsliding, Mass Movement, and Landscape Evolution

Several different types of models have been used to study mass wasting processes. A first category of models simulates landslide propagation using granular physics and fluid mechanics. For example, the D-Claw model (George & Iverson, 2014; Iverson & George, 2014) simulates debris-flow propagation by computing driving and resisting stresses in a two-phase (fluid and granular) mixture. This type of modeling approach produces realistic simulations of mass failure initiation, mobilization, and sediment deposition for individual landslide events. In the context of long-term landscape evolution, however, high-fidelity models of this type have the disadvantage of requiring a large set of model parameters and detailed information on local lithology and hydrology, which are impossible to constrain on the time and space scales relevant to landscape evolution.

A second category of models is commonly referred to as Landscape Evolution Models (LEMs). LEMs combine geomorphic transport laws with mass conservation to create a computational theory for landform evolution over time. These models use relatively simple, time-averaged rate laws for various geomorphic processes to compute the evolution of topography on time scales ranging from decades to epochs (e.g., Tucker & Hancock, 2010). Hillslope evolution is commonly simulated using a diffusion-like sediment-transport law in which transport rate increases (linearly or non-linearly) as a function of topographic gradient (e.g., Andrews & Bucknam, 1987; Roering et al., 1999). In such approaches, landslides are simulated implicitly, either through a mathematical representation in which down-slope material flux accelerates rapidly as the slope gradient approaches a specified threshold, or by simply imposing a maximum possible slope gradient (Campforts et al., 2017; Tucker & Bras, 1998).

A third category of models explicitly simulates landslides by focusing on the mobilization of the uppermost, weathered, layer of Earth's surface. A simplified approach is to combine a steady-state hydrologic model with an infinite slope stability model (Montgomery & Dietrich, 1994). Such an approach is well suited to studying the impact of soil properties and large-scale precipitation variability on the occurrence of shallow landslides (Claessens et al., 2007). Another approach to explicitly model the influence of mass movement on landscape evolution is the use of a glacier-like flow law to simulate deep-seated earthflows in weathered material (Booth et al., 2013). This model is capable of simulating landsliding over large spatial and temporal scales and incorporates both landslide-induced erosion and sediment transport by simulating the occurrence of earthflow-type landslides as a continuum flux of material. Under certain initial and boundary conditions, the model reproduces the stochastic nature of landslides, albeit without explicit triggering mechanics. The simulated landslide flux in the Booth et al. (2013) model depends nonlinearly on the weathered bedrock thickness ($q_s = H^n$, where q_s is the landslide flux, H is the weathered thickness, and n is an empirical exponent). Although this approach enables simulation of earthflows on hillslopes characterized by unlimited weathered rock supply, areas where weathered rock supply is limited and landslides contribute to sediment production require alternative approaches.

A final category of models addresses this challenge by explicitly simulating bedrock landslides (Campforts, Shobe, et al., 2020; Champel, 2002; Densmore et al., 1998; Egholm et al., 2013). These types of models actively simulate production of sediment through mass wasting and thus offer a unique way to investigate the imbalance between gradual soil formation by weathering and episodic sediment production through landsliding. Here, we use this approach, building on the HyLands model (Campforts, Shobe, et al., 2020).

3. The Morphologic Signature of Landsliding

We compare examples of landscapes with and without frequent landsliding to assess the morphological impact of landslides. One landscape, situated on the Appalachian Plateau in south-eastern Ohio (USA), rarely experiences bedrock landslides (Figure 1a). The region is part of the unglaciated section of the Appalachian plateau (Clubb et al., 2014; Fisher et al., 1968). The selected catchment is characterized by rolling topography with elevations ranging between 197 and 315 m above mean sea level and slope gradients with a mode of ca 0.3 m m^{-1} (Figure 1e). The area is underlain by moderately to well drained silt-loam soils, and is covered by mixed-oak forests (Goebel et al., 1996). Although earthflows and rotational slumps do occasionally occur in the area, they are restricted to the weathered zone of the rocks, and deep-seated, bedrock-involved landslides are rare (Fisher et al., 1968). We follow DiBiase et al. (2012) in calculating the extent of the alluvial channel network and corresponding fluvial drainage density. The start of the fluvial channel network is defined at the transition between colluvial and alluvial channels. Colluvial channels are characterized by approximately uniform slope values under increasing
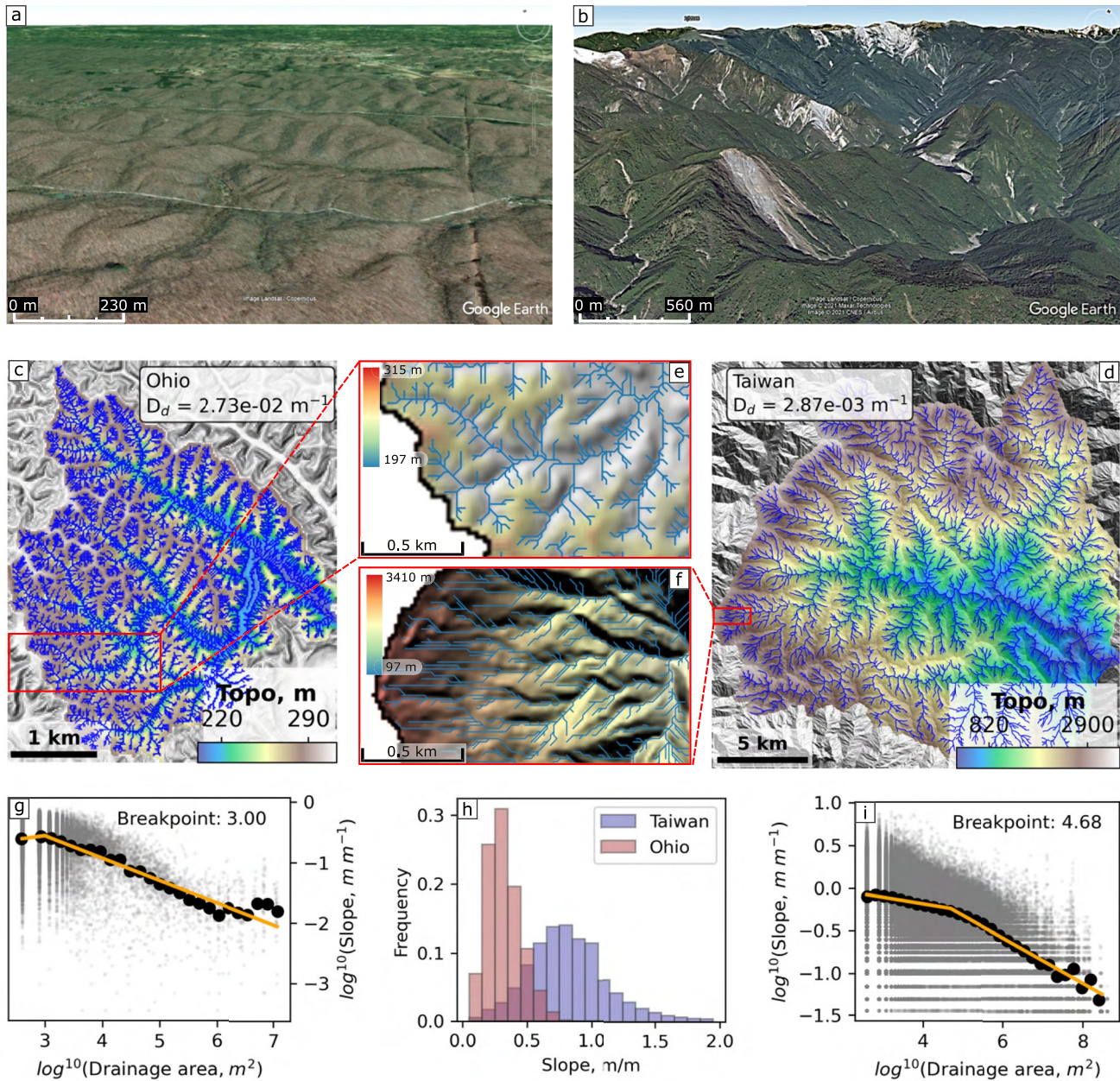
Figure 1. Comparison between landscapes with little to no bedrock landslide activity (Appalachian Plateau, Ohio USA; a, c, e, and g) and with frequent bedrock landsliding (Central Range of Taiwan; b, d, f, and i). The tectonically quiescent Appalachian plateau is dissected by a well-established, mostly dendritic fluvial network (c and e; see also Clubb et al. (2014)). The drainage density (D_d) of the selected catchment (a, 39.43°N; 82.13°W) is calculated using a drainage area threshold for fluvial incision derived from the breakpoint in the slope-area relationship (g; see text). The Taiwan catchment (b, 23.9°N; 121.5°E) is characterized by elongated, quasi-planar hillsides decorated with straight, closely spaced channels (d and f), and has a low drainage density (D_d), as reflected in the relatively large drainage area associated with a breakpoint in the slope-area plot. Black dots in the slope-area plots (g and i) are logarithmic binned averages (Wobus et al., 2006); the orange line represents the best fit obtained using a piece-wise linear regression on the unbinned data. Relative frequency distributions of slope gradients for both catchments are shown in subplot (h) The digital elevation models used in this paper were both resampled to a resolution of 20 m; see "Data Availability" section for details.

drainage area, whereas alluvial channels typically show decreasing slope angles, corresponding to a Flint's law scaling or concave-upward channel profiles (Wobus et al., 2006). In the Ohio catchment the fluvial (alluvial) channel network starts at a drainage area of about 1,000 m², resulting in a relatively high drainage density (D_d) of 0.027 m⁻¹—with D_d calculated using the distance-to-channel method (Tucker et al., 2001).

The second end-member landscape is the central mountain range of Taiwan where deep-seated bedrock landslides dominate hillslope evolution (Hovius et al., 2000). The region experiences high bedrock uplift rates ($\geq$4 mm yr^{-1}) and is densely forested below the tree line (Hovius et al., 2000). The Taiwanese landscape is characterized by steep, quasi-planar, elongated slopes, and is dissected by straight, closely spaced channels (Figure 1f). Steep channels are often buried in meters of landslide-derived sediment which remains in channels for decades after landslide events (DeLisle et al., 2022). The transition between colluvial and alluvial channels occurs farther downstream in comparison to the Appalachian Plateau (at a drainage area of about 48,000 m^2, see Figure 1i) resulting in a drainage density (D_d) of 0.0029 m^{-1}, which is an order of magnitude lower than the value obtained for the Ohio catchment.

While the frequency distribution of slope gradients, calculated on a pixel basis, is characterized by a symmetrical to right-skewed distribution for both catchments (Figure 1h), the slope distribution from the landslide-dominated catchment in Taiwan has a much longer tail. Throughout the paper, Skew is calculated as $3\frac{mean-median}{standard\ deviation}$ where Skew <-0.5 indicates a left-skewed distribution, $-0.5 <$ Skew > 0.5 indicates a symmetrical distribution, and Skew >0.5 indicates a right-skewed distribution. Skew values are 1.01 and 0.36 for Ohio and Taiwan, respectively. Hillslopes in the Taiwan catchment have gradients up to 2 m m^{-1} or 63°, which is far beyond commonly reported values for threshold slopes. This observation hints that threshold slope theory, which predicts that slopes should not exceed a given threshold angle, likely does not fully describe the dynamics of topographic evolution in this landslide-dominated landscape. This is largely due to simplifying assumptions underpinning such models, which do not account for the cohesion that can allow slopes to exceed the angle of internal friction, and temporal variability in landslide triggering mechanisms such as storms and earthquakes, which destabilize slopes by increasing the ratio of driving to resisting stresses (Depicker et al., 2021; Korup, 2008).

4. Methods

4.1. The HyLands Landscape Evolution Model

The HyLands LEM differentiates between bedrock and alluvium/colluvium (Shobe et al., 2017) and explicitly treats stochastic landsliding by combining a Mohr–Coulomb stability analysis with a non-local, non-linear diffusion algorithm (Carretier et al., 2016) to simulate sediment run-out. In comparison to the first release of HyLands (Campforts, Shobe, et al., 2020), the landslide triggering algorithm has been modified by using a Poisson arrival model to represent stochastic trigger events. We also added soil formation and non-linear soil transport to unravel the role of bedrock landslides in the production and mobilization of sediment. The model is summarized below; we refer the reader to Campforts, Shobe, et al. (2020) and Shobe et al. (2017) for the theoretical framework and details on the derivation. The HyLands model is integrated in the open-source Landlab modeling framework (Barnhart et al., 2020b; Hobley et al., 2017), which is part of the Community Surface Dynamics Modeling System (CSDMS) Workbench (Tucker et al., 2021).

4.1.1. Mass Balance

The model represents terrain as consisting of bedrock overlain by a layer of regolith, the thickness of which varies in space and time. Evolution through time of topographic elevation η, bedrock surface elevation R, and mobile regolith thickness H is calculated according to the following mass-balance equations:

$$\frac{\partial \eta}{\partial t} = \frac{\partial R}{\partial t} + \frac{\partial H}{\partial t} \tag{2}$$

$$\frac{\partial R}{\partial t} = U - E_{r_{fluv}} - P_0 e^{-H/H^*} - E_{r_{ls}} \tag{3}$$

$$\frac{\partial H}{\partial t} = \left(\frac{1}{1-\phi_{sed}}\right)\left(P_0 e^{-H/H^*} + D_{s_{ls}} + D_{s_{fluv}} - E_{s_{ls}} - E_{s_{fluv}}\right) - \nabla \cdot \mathbf{q}_s. \tag{4}$$

Rock uplift rate relative to baselevel is represented by U $[L\ T^{-1}]$ and sediment porosity by ϕ_{sed}. $E_{r_{fluv}}$ $[L\ T^{-1}]$ represents fluvial bedrock erosion rate as a volume flux per unit bed area while $E_{s_{fluv}}$ $[L\ T^{-1}]$ represents sediment entrainment and $D_{s_{fluv}}$ $[L\ T^{-1}]$ is the fluvial deposition flux. $\mathbf{q}_s = \mathbf{q}_f + \mathbf{q}_h$ $[L^2\ T^{-1}]$ represents the combined flux of sediment (mobile regolith) due to fluvial transport, $\mathbf{q}_f$, and soil creep, $\mathbf{q}_h$. P_0 represents the maximum soil formation rate under zero soil thickness $[L\ T^{-1}]$ and H^* is the soil production decay depth [L]. Landsliding causes

bedrock erosion given by the volumetric flux per area $E_{r_{ls}}$ $\left[L\,T^{-1}\right]$ as well as sediment entrainment given by the volumetric flux per area $E_{s_{ls}}$ $\left[L\,T^{-1}\right]$ and deposition given by the volumetric flux per area $D_{s_{ls}}$ $\left[L\,T^{-1}\right]$.

4.1.2. Fluvial Incision, Transport, and Deposition

Fluvial bedrock incision, sediment transport, and deposition are calculated using the SPACE model (Shobe et al., 2017) where:

$$E_{s_{fluv}} = K_s q S^n \left(1 - e^{-H/H_{*fluv}}\right) \tag{5}$$

represents sediment entertainment and

$$E_{r_{fluv}} = K_r q S^n e^{-H/H_{*fluv}} \tag{6}$$

represents bedrock erosion. K_s and K_r $[L^{-1}]$ are erodibility constants for sediment and rock, respectively. q represents water discharge per unit width and is calculated as $q = k_q A^m$, where k_q is a coefficient subsumed into the coefficients K_s and K_r, and m is the drainage area exponent. S represents the channel slope $[L\,L^{-1}]$ and n is the slope exponent. The thickness of bed sediment H $[L]$ relative to some bedrock roughness length scale H_{*fluv} $[L]$ sets the extent to which sediment entrainment or bedrock erosion dominates at any given time and place. Note that the model does not distinguish between different types of unconsolidated granular material, such as actively water-worked channel-bed sediment, colluvium on hillslopes, or older alluvial sediment in terrace-like features. All of these types of materials are considered to be lumped together in the general category of "regolith," the thickness of which is represented by H.

We follow Davy and Lague (2009) and calculate the sediment deposition flux as:

$$D_{s_{fluv}} = \frac{Q_{s_{fluv}}}{Q} V. \tag{7}$$

where $D_{s_{fluv}}$ $\left[L\,T^{-1}\right]$ is the deposition flux, $Q_{s_{fluv}}$ $\left[L^3\,T^{-1}\right]$ represents the volumetric sediment discharge, Q $\left[L^3\,T^{-1}\right]$ is the volumetric water discharge, and V $[L\,T^{-1}]$ is the effective sediment settling velocity. Erosion does not occur within closed topographic depressions created by landslide dams. Within these depressions, which represent landslide-dammed lakes, sediment settling velocity is specified by V_{lake}. The priority-flood flow routing algorithm is used to route water over the terrain and identify dammed areas (Barnes et al., 2014).

4.1.3. Soil Formation and Non-Linear Soil Creep

Conversion of bedrock into mobile regolith by weathering processes is represented using an exponential function of local regolith thickness, as indicated by the third term on the right side of Equation 4. Soil creep over hillslopes is simulated using a nonlinear depth-dependent transport law. Following Ganti et al. (2012) and Barnhart et al. (2019), a truncated Taylor series approximation is used to represent a super-linear increase in flux as gradient approaches a specified critical value, S_c. The approach of Johnstone and Hilley (2015), which assumes an exponential soil creep velocity profile, is used to represent the influence of mobile regolith cover thickness on transport rate. Combining these, the soil flux ($\mathbf{q}_s$, $[L^2 T^{-1}]$) can be written as:

$$
\begin{aligned}
\mathbf{q}_s \quad = \quad & -D\nabla\eta \left(1 - \exp\left(-\frac{H}{H_{*diff}}\right)\right) \\
& \left(1 + \left(\frac{S}{S_c}\right)^2 + \left(\frac{S}{S_c}\right)^4 + \cdots + \left(\frac{S}{S_c}\right)^{2(N-1)}\right)
\end{aligned}
\tag{8}
$$

where $S = |\nabla\eta|$ $\left[L\,L^{-1}\right]$ is the magnitude of topographic slope gradient, H_{*diff} $[L]$ is a characteristic soil depth for which soil creep decreases to $\left(1 - \frac{1}{e}\right)$ of its maximum value, D $[L^2\,T^{-1}]$ is the diffusion coefficient, and S_c is the critical gradient. N represents a user-defined number of terms to be used in the Taylor series expansion (Barnhart et al., 2019).
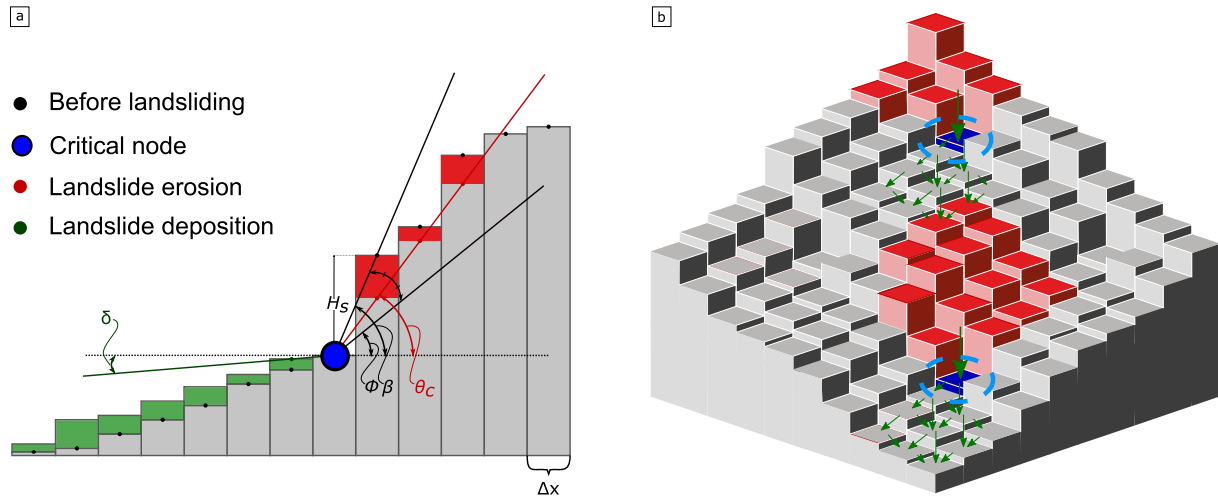
Figure 2. (a) Two-dimensional representation of landslide erosion and deposition. The Culmann approach (Culmann, 1875) is used to calculate landslide erosion (the red shaded area). At failure, the rupture angle θ is bisecting the topographic slope (β) and the angle of internal friction (ϕ). The green shaded area represents deposition of the landslide-derived sediment. Landslide sediment run-out is calculated using a non-local diffusion equation (Equation 17). Optionally, a minimal deposition surface angle (δ) can be considered when redistributing the sediment over the hillslope. (b) Three-dimensional representation of landslide erosion and sediment run-out. Blue cells highlighted with blue dotted lines, indicate critical locations where landslides initiate, corresponding to the critical node in (a). Red cells represent landslide erosion, as calculated using the Culmann approach whereas green arrows indicate sediment run-out and deposition over downslope cells. Figure adjusted from Campforts, Shobe, et al. (2020).

4.1.4. Landslide Triggering

We developed a probabilistic model to predict the number of landslides over a given time span, and the given information on the stability of a slope. We aim to combine information regarding the temporal probability of landslides (events triggering landslide activity) and the spatial probability of landslides—following the Culmann criterion for landsliding, (e.g., Densmore et al., 1998). HyLands models the probability of failure p_{fail} as:

$$p_{fail} = P_t \times P_s. \tag{9}$$

where P_t is the probability that a potential trigger event will occur during a specified time interval and P_s is the probability that failure will occur at a specified location given the occurrence of a potential trigger event. p_{fail} is calculated for every cell, and it gives the probability that a cell will be converted into a critical sliding node (Figure 2). The area and volume of landslides are not defined statically but evolve physically from the model.

4.1.4.1. Temporal Probability: Poisson Model

We use a Poisson model to predict the temporal probability of landslide occurrence. The goal is to derive the probability P of having $N(t) \geq 1$, where $N(t)$ is the number of landslides during time interval t. Temporal probabilities are calculated by assuming that landslides are random point-events. Following Crovelli (2000), the probability of N landslides on a conditionally unstable slope during a time interval t can be expressed as a Poisson distribution:

$$f(n; \lambda t) = P\{N(t) = n\} = e^{-\lambda t}\frac{(\lambda t)^n}{n!}. \tag{10}$$

where n is the number of landslide occurrences and λ is the mean rate of landslide occurrences. Note that λ is the reciprocal of the mean recurrence interval between landslide triggering events, t_{LS}. From Equation 10, we can calculate the probability of having no landslides ($n = 0$) during time t as

$$P\{N(t) = 0\} = e^{-\lambda t}. \tag{11}$$

and so it shows that the probability of having at least one or more landslides is

$$P_t = P\{N(t) \geq 1\} = 1 - e^{-\lambda t} = 1 - e^{\frac{-t}{t_{LS}}}. \tag{12}$$

Landslide triggering is implemented numerically by using Equation 12 to calculate the probability of a trigger event in each model time step of duration dt.

4.1.4.2. Spatial Probability: Culmann Theory

Following Culmann theory (Culmann, 1875), we know that the probability of failure depends on the ratio of the hillslope height H_s and the maximum stable hillslope height H_c:

$$P_s = \frac{H_s}{H_c}. \tag{13}$$

where P_s is the spatial probability for failure, H_s is the local hillslope height calculated as the difference between every cell in the landscape and its highest neighbor, and H_c is the maximum stable hillslope height, which is calculated as (Champel, 2002; Densmore et al., 1998):

$$H_c = \frac{4C}{\rho\, g} \frac{\sin\beta \cos\phi}{1 - \cos(\beta - \phi)}. \tag{14}$$

Here, C is the cohesion [ML^{-1} T^{-2}], ρ is the rock density [ML^{-3}] set to 2,700 kg m^{-3}, g is gravitational acceleration ($g = 9.81$ ms^{-2}), β is the local topographic angle, and ϕ is the material's angle of internal friction. A visual representation of the spatial probability for sliding is provided in Figure 2.

4.1.4.3. Combined Probability

Substituting Equations 12 and 13 into Equation 9 results in a general formulation for the probability of failure to occur at a given location (x, y) over a time interval t:

$$p_{fail} = \left(1 - e^{\frac{-t}{t_{LS}}}\right) P_s(x, y). \tag{15}$$

4.1.4.4. Stochastic Simulation of Landslides

Every model iteration, Equation 9 is updated for all cells where the topographic gradient (β) exceeds the critical material friction angle (ϕ). Grid cells where landslides initiate are selected by generating a uniformly distributed pseudorandom number r between 0 and 1. If $r \leq p_{fail}$ for a particular cell, a landslide will occur. Landslides cannot overlap: during one model time-step every node of the modeled domain can only be part of one unique landslide. Technical details on the implementation of the landslide algorithm are provided in Campforts, Shobe, et al. (2020).

4.1.5. Landslide Erosion

Landslide erosion of sediment $\left(E_{s_{ls}}\right)$ and bedrock $\left(E_{r_{ls}}\right)$ by gravitational slides is calculated as a stochastic event process. When a trigger event occurs (Section 4.1.4), the volume of material removed in a landslide is calculated on the basis of a Culmann stability model, assuming Mohr-Coulomb materials, where a failure plane with a dip angle θ_c bisects the local topographic angle β, and the material's angle of internal friction ϕ (Champel, 2002; Densmore et al., 1998b):

$$\theta_c = \frac{\beta + \phi}{2}. \tag{16}$$

The Culmann theory is used to calculate the areal extent and volume of individual landslides (Figure 2a). When a landslide is initialized at a critical node, the rupture plane will propagate toward the surface until it intersects topography. Propagation is simulated using a recursive algorithm that starts at the critical node and evaluates whether the angle toward any of its neighboring cells (β) exceeds the dip angle (θ_c, Equation 16). If this is the case, the elevation of the neighboring node is lowered so that $\beta = \theta_c$. The impacted cell is now considered a landslide node itself and the same procedure is iterated for all of its neighboring nodes until β nowhere exceeds θ_c for a continuous patch of nodes initialized at the critical sliding node. Landslide area and volume are calculated for each individual slide by summing up, respectively, the number of cells impacted by landslides and the volume of material eroded per cell.

4.1.6. Landslide Sediment Run-Out and Deposition

Landslide-derived sediment is redistributed over the hillslope and deposited using a non-linear, non-local deposition scheme (Carretier et al., 2016):

$$D_{s_{ls}} = \frac{Q_{s_{ls}}/w}{L} \tag{17}$$

where $D_{s_{ls}}$ $[L\,T^{-1}]$ represents the deposition flux per area and $Q_{s_{ls}}$ $[L^3\,T^{-1}]$ represents the volumetric landslide-derived sediment discharge. The transport distance L [L] is calculated as:

$$L = \frac{dx}{1 - \left(\frac{S}{Sc}\right)^2} \tag{18}$$

where S is the slope angle $[L\,L^{-1}]$, dx is a reference length scale for transport distance on a flat surface here set to Δx, and S_c is a theoretically derived critical slope gradient $[L\,L^{-1}]$. In our simulations, we assume S_c to be equal to the tangent of the angle of internal friction (ϕ). We use a multiple flow direction algorithm (Barnes et al., 2014) to redistribute sediment over the downstream cells proportionally to their slope (Figure 2b). Once landslide-derived sediment hits dammed areas, sediment will be deposited until the lake is filled or until the sediment flux is depleted.

4.2. Numerical Experiments

We assess the role of landslides in altering the morphological and temporal evolution of landscapes by performing numerical experiments in which the landscape reaches a dynamic equilibrium between erosion and rock uplift. We represent the two real-world cases presented in Figure 1 by comparing simulated landscape evolution under different degrees of landslide activity. Varying landslide activity can be generated in different ways: increasing landscape relief, increasing landslide triggers, or changing rock material properties. Because we aim to evaluate the impact of landslides on quasi-equilibrium topography, we control relief by varying rock uplift rates on a linear scale between $U = 10^{-4}$ m yr^{-1} (scenario 1) and $U = 10^{-3}$ m yr^{-1} (scenario 8). Parameters controlling fluvial incision include rock and sediment erodibility (K_r and K_s) and the area and slope exponents (m and n), which are set to 10^{-5}m^{-1}, 1.5×10^{-5}m^{-1}, 0.45, and 1. In all model runs the value of H_{*fluv} is set to 0.1 m. The maximum soil formation rate (P_0) and the soil production decay depth ($H*$), are set to 3×10^{-4} m yr^{-1} and 0.44 m, respectively. Parameters controlling non-linear, depth-dependent soil creep over hillslopes include the transport coefficient (D) and the soil transport decay depth (H_{*diff}). For all model runs, D and H_{*diff} are set to 0.01 m^2 yr^{-1} and 0.1 m, respectively. Parameters controlling the spatial occurrence and magnitude of landslides include tangent of the angle of internal friction and cohesion, which are set to 1.2 mm^{-1} and 15 kPa, respectively. The frequency of potential trigger events is controlled by the mean recurrence interval between landslide triggering events, here set to 10^4 yrs. A complete list of parameter values is provided in Table 1.

4.3. Topographic Metrics

We use a set of topographic metrics to interpret numerical findings and compare them to actual landscapes. A first metric is the drainage density, D_d $[L^{-1}]$, which is calculated using the distance-to-channel method (Tucker et al., 2001). The extent of the fluvial network used to calculate D_d is determined using a drainage area threshold for fluvial incision derived from the breakpoint in the slope-area relationship (Section 3). A second metric is the area-normalized stream concavity index (SCI; see Demoulin, 1998). Positive SCI values are equivalent to concave profiles while negative values indicate convex profiles. Details on the derivation and interpretation of the SCI metric can be found in Zaprowski et al. (2005). A third metric is the normalized river steepness (k_{sn}), which is the upstream area-weighted channel gradient: $k_{sn} = SA^{m/n}$, where A is the upstream drainage area, S is the channel slope, and the value of m/n is set to 0.45 (Wobus et al., 2006).

Table 1
Parameter Values for HyLands Model Runs

|		Main simulations
Parameter	Description	Figures 5 and 6
Rows (−)	Number of grid rows	300
Columns (−)	Number of grid columns	240
Δx, Δy (m)	Cell spacing	50
Δt (yr)	Time step	500
T_{tot} (Myr)	Total run time	225
H_{ini} (m)	Initial soil thickness	0
U (m yr^{-1})	Uplift rate	Varying per scenario
K_r (m^{-1})	Bedrock erodibility	1×10^{-5}
K_s (m^{-1})	Sediment erodibility	1.5×10^{-5}
m (−)	Slope exponent	0.45
n (−)	Area exponent	1
H_{*fluv} (m)	Bedrock roughness length scale	0.1
ϕ_{sed} (−)	Porosity of the bed sediment	0
$F_{f\,fluv}$ (−)	Fraction of fine fluvial sediment	0
V (m yr^{-1})	Effective settling velocity	1
V_{Lake} (m yr^{-1})	Effective settling velocity in lakes	1
P_0 (m)	Maximum soil production rate	3×10^{-4}
H_* (m)	Soil production decay depth	0.44
D (m^2 yr^{-1})	Diffusion coefficient	0.01
H_{*diff} (m)	Characteristic soil depth for soil creep	0.1
C (kPa)*	Cohesion	15
ϕ (mm^{-1})	Tangent of the angle of internal friction	1.2
t_{LS} (yr)**	Mean recurrence interval between landslide trigger events	1×10^4
δ (mm^{-1})	Tangent of the minimal deposition angle	0.01
$F_{f\,hill}$ (−)	Fraction of fine hillslope sediment	0

Note. *C varies for simulations shown in Figure 6c. ** t_{LS} varies for simulations shown in Figure 6b.

5. Results

### 5.1. The Topographic Structure of Landslide Terrain

Under relatively low rock-uplift rates (Figure 3, scenario 1), a steady-state topography emerges in which slope gradients are too gentle to trigger frequent landsliding. Erosion rate and sediment cover are uniform across the domain (Figure 3e). The slope-area relationship (Figure 3i) displays a rollover in which slope first increases with increasing drainage area and then decreases linearly with increasing drainage area in log-log space. This modeled slope-area relationship resembles the pattern seen in the real-world case with gentle topographic relief (Figure 1g), and commonly observed in other moderate-gradient, soil-mantled landscapes (Montgomery & Foufoula-Georgiou, 1993). In the model experiments, the rollover represents a shift from creep-dominated hillslopes to fluvially influenced valleys. When rock uplift rate is low (scenarios 1, 2, and 3), slow fluvial incision prevents the formation of slope gradients that exceed the angle of internal friction, thereby preventing landslide activity. The predominance of below-threshold slopes can be seen in the slope histogram (Figure 3m), which show maximum gradient values of ca. 0.3 m m^{-1}. The left-skewed histogram (Skew = −0.81) represents a landscape that is characterized by concave-upward streams and convex-upward hillslopes.

With increasing uplift rates, the landscape steepens and landslides start to occur. The occurrence of individual landslide events is shown in Figure 4. Given the set of selected parameter values (Table 1), landslides occur for
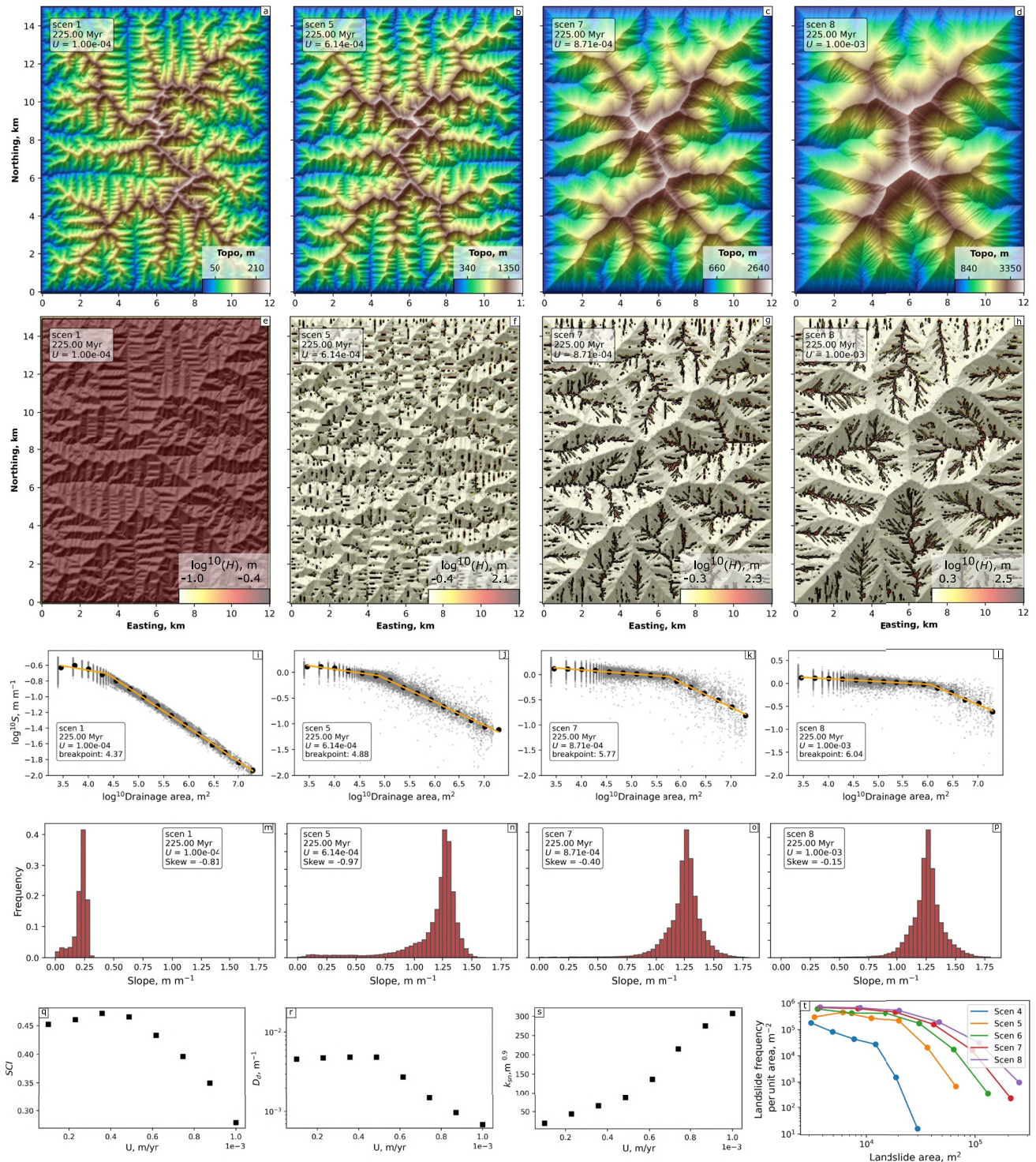
Figure 3. The role of landslides in shaping topography under varying rock uplift rates. (a–d) Topographic elevation after 225 million model years for uplift of 1×10^{-4}, 6.14×10^{-4}, 8.71×10^{-4}, 1×10^{-3} m yr^{-1}, respectively. (e–h) Sediment thickness evolves to spatially uniform values when no landslides occur (e), while landslide activity strongly redistributes sediment and results in aggradation or terracing in fluvial channels and valleys (f–h). (i–l) Slope-area plots; black dots are logarithmic binned averages and the orange line represents the best fit obtained using a piece-wise linear regression on the unbinned data. (m–p) Slope histograms. (q) Stream concavity of trunk river (SCI). (r) Drainage density (D_d). (s) River steepness (k_{sn}). (q–s) Values calculated at dynamic equilibrium (225 Myr) for the range of simulated uplift rates. (t) Magnitude frequency distribution of landslides between 221 and 225 million model years. No landslides occur under low rock uplift rates (scenarios 1–3), the plotted lines indicate scenarios 4–8, in which landsliding does occur. See Movie 1 for a dynamic representation.
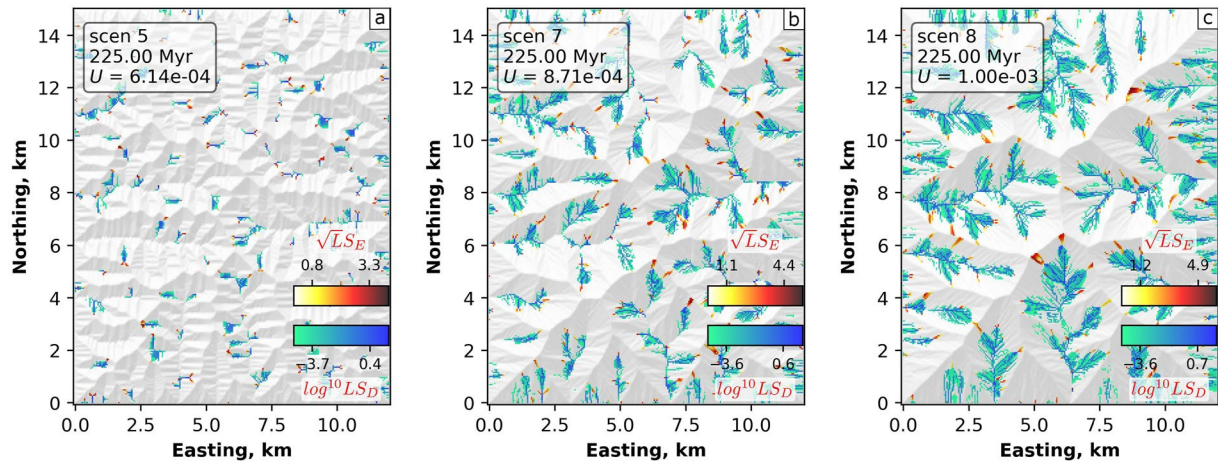
Figure 4. Instances of landslides during the last 2.5×10^5 years at dynamic equilibrium. Red colors represent the square root of landslide erosion (LS_E, m), blue shades show the common logarithm of landslide sediment runout and deposition (LS_D, m). Model scenarios correspond to those shown in Figure 3.

scenarios where $U > 0.4$ mm yr^{-1} (scenario 4). Landslides plotted in Figure 4 represent all the occurrences over the last 2.5×10^5 years of each model run. In scenarios with modest relief, landslide erosion patches are small, and the resulting sediment spreads out to form colluvial cones. Steeper landscapes (scenarios 7 and 8) are characterized by larger landslide erosion scars. In these steep landscapes, sediment is routed downslope over hillslopes and accumulates in the fluvial network. In steep landscapes, landslide-produced sediment travels far because slopes approach the landscape threshold slope (S_c), resulting in large transport distances (Equation 18).

At high rock uplift rates, topographic gradients locally exceed the tangent of the angle of internal friction (1.2 mm^{-1}, Figure 3, scenarios 5, 7, and 8) causing increased frequencies and magnitudes of landslide activity (Figure 3t). Landslides cause the formation of elongated, quasi-planar hillslopes bearing closely spaced, quasi-parallel, channel-like features (Figures 3c and 3d). Such incision occurs because sufficient time elapses between landslide events for channels to develop on former landslide failure planes. In the slope-area plots, the region dominated by mass failures and modulated by minor channel incision can be recognized as the relatively flat region where slope gradient decreases only modestly with increasing area (Figures 3j, 3k, and 3l). This regime expands as uplift rates increase, resulting in greater area values for the automatically identified breakpoints in the slope-area plots. The model runs are consistent with observed slope-area patterns, and with the reduced drainage density in landslide-prone Taiwan as compared with the lower-relief setting of the Appalachian Plateau (Figure 1). Moreover, the stochastic landsliding model accounts for conditionally unstable hillslope gradients that persist for some period of time before they fail, leading to a more symmetrical slope frequency distribution for model scenarios receiving high uplift rates (Figures 3o and 3p, Skew = −0.40 and −0.15, respectively).

The transition between low and high uplift rates is reflected by the stream concavity index (SCI; see Demoulin, 1998), which is ca. 0.45–0.5 at low uplift rates (Figure 3q) representing strongly concave upward profiles (Zaprowski et al., 2005). For $U \geq 4 \times 10^{-4}$ m yr^{-1}, SCI values start to decrease, reflecting the influence of landsliding on longitudinal profile morphology. The overall concavity (SCI value) of channel profiles decreases as landslides provide large volumes of sediment to the lower reaches of fluvial channels that are not evacuated instantaneously. While upstream fluvial reaches are steep enough to facilitate rapid sediment transport, downstream reaches are characterized by a lower river gradient resulting in aggradation of landslide-derived material. The impact of landsliding is also reflected in steepness values (k_{sn}) shown in Figure 3s. k_{sn} values increase almost linearly with low uplift rates ($U < 0.5 \times 10^{-3}$ m yr^{-1}) but increase nonlinearly with faster rock uplift, once landslides start perturbing fluvial channels. At high uplift rates ($U > 0.8$ mm yr^{-1}), k_{sn} flattens out and evolves toward a maximum value. This maximum value is imposed by the angle of internal friction which will eventually turn all landscape parts into landslides under very high uplift rates (not shown here). Drainage densities (D_d) are solely controlled by fluvial incision and soil creep as long as uplift rates are smaller than 4×10^{-4} m yr^{-1}, resulting in near-constant values for drainage density (Figure 3r). Once uplift rates exceed 4×10^{-4} m yr^{-1}, D_d decreases nonlinearly with increasing uplift rates and the commensurate rise in landslide activity.

5.2. Spatial Patterns of Landslide Erosion and Deposition

In experiments in which the maximum rate of mobile regolith production by weathering (P_0) exceeds the rock uplift rate (U), the regolith thickness evolves into a steady, spatially uniform pattern (Figure 3e). Spatial uniformity in regolith thickness reflects an equilibrium adjustment in which the regolith is everywhere just thick enough to allow bedrock weathering to balance the uplift rate. When the rock uplift rate exceeds the maximum rate of soil production by weathering (here 3×10^{-4} m yr^{-1}), soil production can no longer keep pace with increasing relief. In this case, a combination of bedrock landsliding and fluvial erosion of bedrock is required to maintain equilibrium between erosion and rock uplift. At dynamic equilibrium, the mobile regolith thickness ceases to be spatially uniform and sediment dominantly accumulates in and around the valley network (Figures 3f–3h).
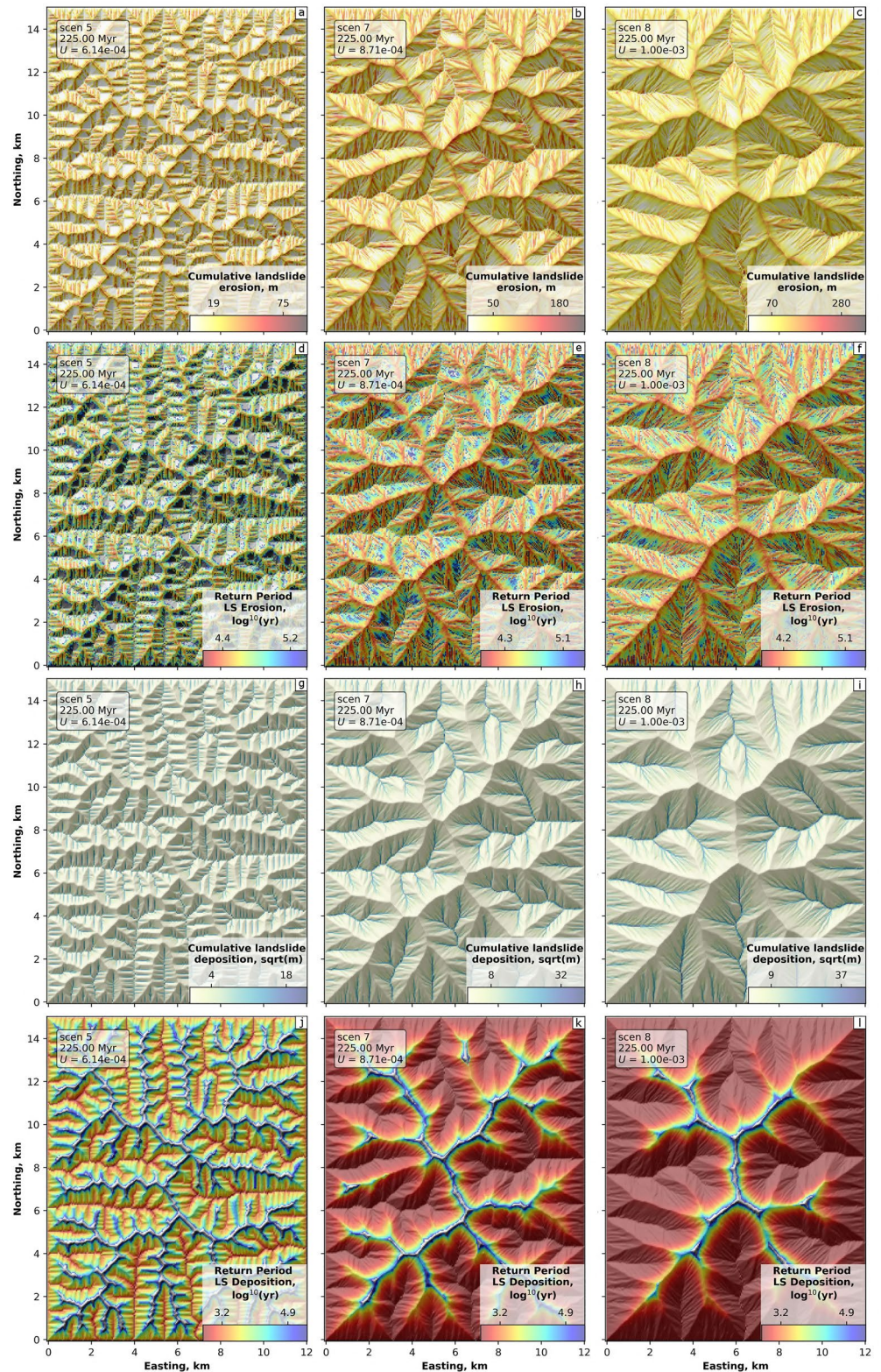
Landslide erosion and deposition vary spatially throughout the experimental landscapes. Figure 5 shows cumulative erosion and deposition rates due to landsliding integrated over the last 2.5×10^5 years of the total model run at dynamic equilibrium. Landslide erosion predominantly occurs closer to ridges, reflecting the greater steepness of the terrain in these regions. Note that the spatial pattern of landslide erosion depends on topographic terrain. In rolling terrain with less steep ridges, landslides will occupy the steeper parts of the landscape. When the uplift rate is larger than the maximum weathering rate, mobile regolith tends to be evacuated from the hillslopes faster than it can be produced, resulting in steep slopes with little or no regolith cover. These regions will be prone to landsliding: when integrated over the timescales plotted in Figures 5a–5c, most areas near the divide will slide. This is also represented in the maps illustrating the return time for landslides (Figures 5d–5f); areas close to ridges are characterized by return times between 1,000 and 10,000 years, while regions closer to the valley network can have return periods up to 5×10^5 years. The return period for landsliding at a given point differs from the model parameter t_{LS}, which controls the recurrence interval between landslide trigger events. t_{LS} influences the frequency at which oversteepened slopes in the landscape will fail, but the actual occurrence of landsliding at a given point depends on its gradient and on the characteristics of the surrounding terrain.

When considering spatial patterns of landslide deposition integrated over the last 2.5×10^5 years of the total model run at dynamic equilibrium (Figures 5g–5i), most of the landslide-derived sediment is deposited in and around the valley network. In the landslide-prone experimental landscapes, slopes are steep and quasi-planar and because of the nonlinear dependence of downslope sediment flux on gradient (Equation 18), the slopes provide a "highway" for sediment to travel from mountain tops to valleys. The preferential accumulation of sediment in valleys is reflected in maps showing the return periods for landslide deposition (Figures 5j–5l). Deposition is negligible on and near ridges, but high (frequent deposition) and relatively spatially uniform on lower slopes and in valleys.

## 5.3. Landslide Frequency Controls Landscape Slope Distributions

While the landslide-prone model runs produce landscapes with a modal slope close or equal to the tangent of the angle of internal friction (1.2 m m^{-1}), the extent of the right tail of the slope distribution is controlled by the probability for critical slopes to fail, p_{fail} (Equation 9). p_{fail} is controlled by a temporal probability for failure (Equation 12), which is governed by the mean recurrence interval for landslide trigger events (t_{LS}), and by a spatial probability for failure (Equation 13), which is governed by the cohesion (C) of the substrate in which landslides occur. Changing parameter values for t_{LS} and C alters model behavior in a similar way. To investigate the impact of landslide frequency on slope distributions, we plot the frequency of hillslope gradients (Figures 3m–3p) as a cumulative distribution (Figure 6). In a first experiment, we evaluate the impact of varying uplift rates using similar values for t_{LS} and C (Figure 6a). When the rock uplift rate is low (scenario 1), landscape evolution is dominated by fluvial and soil-creep processes. For higher uplift rates, episodic landsliding starts to occur. Although the tangent of the angle of internal friction is fixed at 1.2 m m^{-1} for all model runs, several hillslope pixels exceed this value.

In the second and third modeling experiment, we evaluate the impact of changing t_{LS} and C, respectively (Figures 6b and 6c). The fraction of slope gradients that exceed the angle of internal friction at dynamic equilibrium is controlled by the mean recurrence interval for landslide trigger events (t_{LS}). With increasing recurrence times, the chances of a landslide occurring at any given time decrease (Equation 12). Cohesion (C) has a similar effect on controlling landslide frequency (Figure 6c). High values for C will increase the maximum stable

Figure 5. Spatial and temporal patterns of landslide erosion and deposition. (a–c) Cumulative erosion integrated over 2.5×10^5 years at dynamic equilibrium. (d–f) Return period of landslide erosion at dynamic equilibrium, calculated over 2.5×10^5 years. (g–i) Cumulative deposition integrated over 2.5×10^5 years at dynamic equilibrium. (j–l) Return period of landslide deposition at dynamic equilibrium, calculated over 2.5×10^5 years.
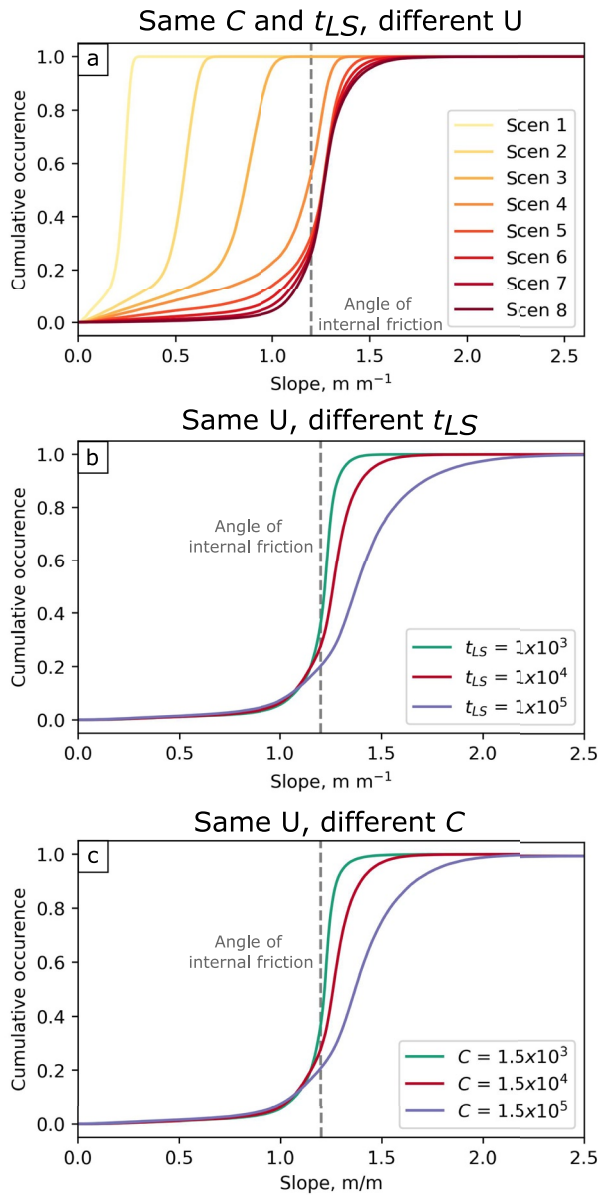
Figure 6. Cumulative frequency distribution of slopes for model scenarios shown in Figure 3. (a) Under low rock uplift rates (scenario 1), landscape evolution is controlled by fluvial incision because the landscape is not steep enough for landslides to occur. With increasing rock uplift rates (with scenario 8 representing the highest uplift rate), the overall slope gradients increase. Because we explicitly simulate the episodic nature of landslides, slope gradient values can evolve beyond the tangent of the angle of internal friction of 1.2 m m^{-1} used in all simulations. The extent to which oversteepened slope patches persist in the landscape depends on the mean recurrence interval for landslide trigger events, t_{LS}. This is shown in (b) where the impact of varying t_{LS} on cumulative distribution of slope gradients is evaluated. The scenario plotted in this graph is scenario 7, corresponding to a high uplift rate of 8.71×10^{-4} m yr^{-1}. With increasing recurrence times for landslide triggering events, chances of actual landslide initiation decrease, resulting in more slope patches that are steeper than the angle of internal friction. (c) Shows the impact of varying values for cohesion, C. Similar to t_{LS}, high values for cohesion increase the rock strength and decrease the chances of triggering a landslide.

hillslope height and do decrease the spatial probability for landslides to occur (Equations 13 and 14). Note that Figures 6b and 6c are almost identical given the similar effect of t_{LS} and C for the illustrated model setups.

5.4. Persistent Landscape Dynamism

Sediment mobilization by landslides has effects that cascade down through the landscape (Fan et al., 2019). Because HyLands simulates landslide dynamics on geological timescales using a non-linear diffusion algorithm to spread out landslide-derived sediment instantaneously after landslide occurrence (Campforts, Shobe, et al., 2020), sediment is mobilized rapidly over steep hillslopes and deposited in less steep fluvial valley floors (Figure 3h). The influences of landslide-derived sediment on fluvial dynamics are three-fold (Figure 7): (a) landslide sediment covers valley-floor bedrock, resulting in reduced river incision rates, (b) it may block the channel, forming a landslide dam (Figure 7f), and/or (c) it diverts the river from its former bed, resulting in the formation of epigenetic river gorges that erode their former valley walls (Figure 7g, see also Ouimet et al., 2008). Episodic delivery of sediment into rivers also triggers the formation of autogenic knickpoints both directly, through the formation of epigenetic gorges and/or landslide dams that fill the valley, and indirectly by temporarily shielding individual reaches of bedrock valley floor from incision. Integrated over geological timescales, sediment delivery to fluvial channels decreases the concavity of fluvial channels, as seen in Figures 7a versus 7d and reflected in the concavity index shown in Figure 3q. Less pronounced fluvial concavity arises because (a) landslide-derived sediment preferentially deposits in the less steep fluvial parts of the landscape where rivers have to carve their way through the sediment before they can resume incising bedrock (Figure 3h) and (b) because the presence of landslide dams inverts fluvial slopes temporally, inhibiting fluvial incision.

Landslide occurrence strongly enhances fluvial channel mobility through time. Figures 8a and 8b compare the mobility of fluvial channels through time for model Scenario 1 with low uplift rates and no landslides versus Scenario 7 undergoing high uplift and landslide rates.

To quantify the mobility of fluvial channels, we developed a new fluvial mobility index based on the transition of model cells between fluvial and non-fluvial states. For each time step, the location of fluvial channels is determined using a fixed drainage area threshold of 1×10^5 m^2. The model then compares the number of pixels that went from a "river" state (defined as having a drainage area that exceeds the imposed threshold) to a "no-river" state (cells in which the drainage area falls below the threshold) or from a "no-river" state to a "river" state and takes the maximum of those two values. From this, we calculate the percentage of river cells that change status every iteration:

$$M_{riv} = \frac{\max\left((C_r \to C_{nr}), (C_{nr} \to C_r)\right)}{dt \times C_r}. \tag{19}$$

Here, M_{riv} is the mobility index (% change per year), C_r represents the total number of river cells, and C_{nr} is the total number of non-river cells. M_{riv} indicates the percentage of the fluvial network that shifts status per unit of time but does not capture the length over which channels migrate. In the absence of landslides (Figure 8a), mobility is high in the first time steps during which the fluvial channels are being imprinted, and subsequently approaches 0% as
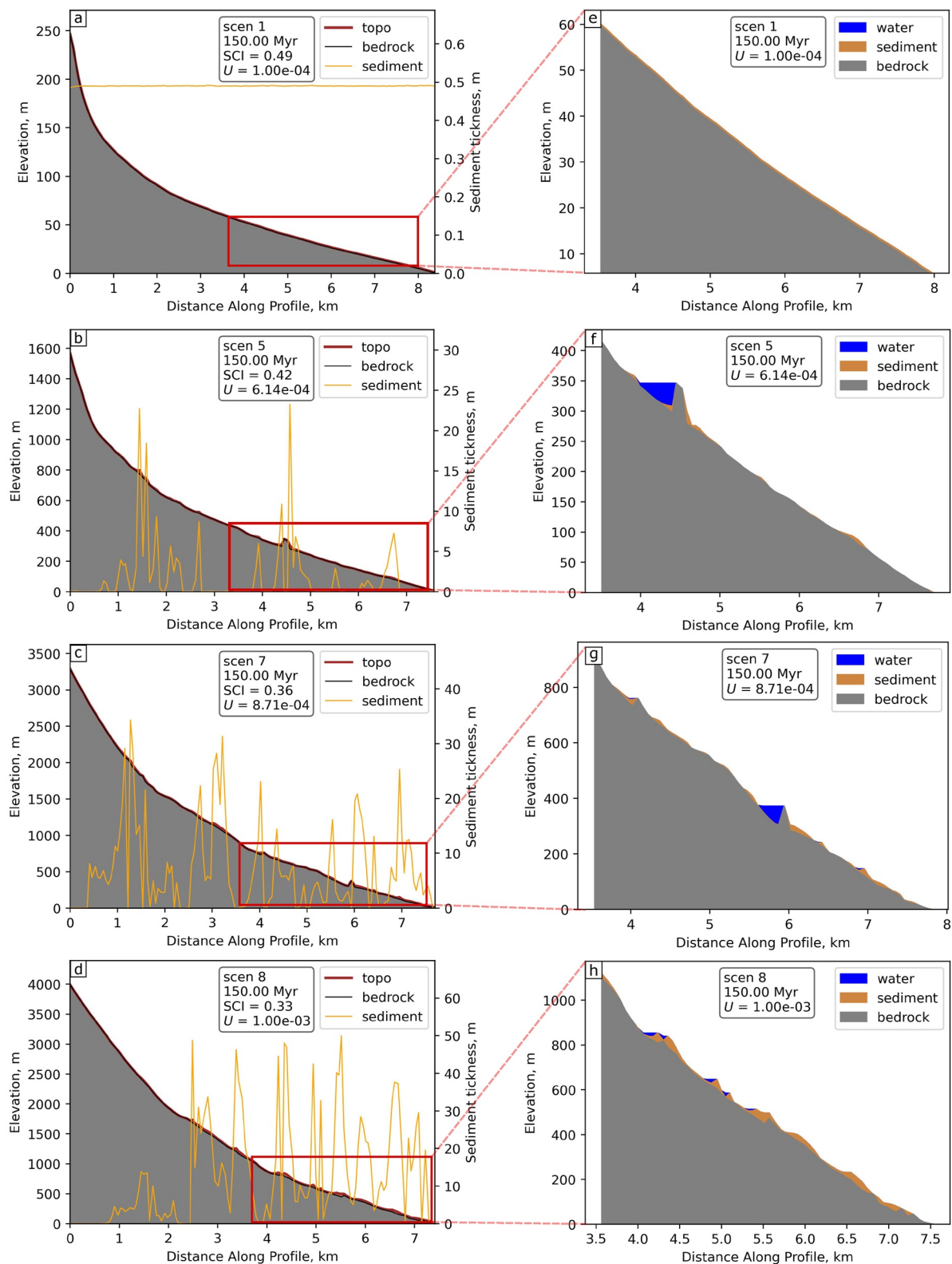
Figure 7. Longitudinal river profiles along the trunk stream after 225 million model years for selected uplift scenarios 1, 5, 7, and 8 (a–d). The gray shaded area represents the bedrock and the red line represents topography (bedrock + sediment thickness). The yellow line represents sediment thickness, plotted on the right *y* axis. (e–h) Zoom into selected parts of the profiles indicated with red squares in (a–d). Blue shaded areas upstream of yellow bumps (sediment dams) indicate the presence of a landslide-dammed lake. Gray bumps represent epigenetic gorges. Note that water depths are not explicitly simulated; and water discharge is assumed proportional to the contributing drainage area at any point in space (Section 4.1.2). See Movie 2 for a dynamic representation.
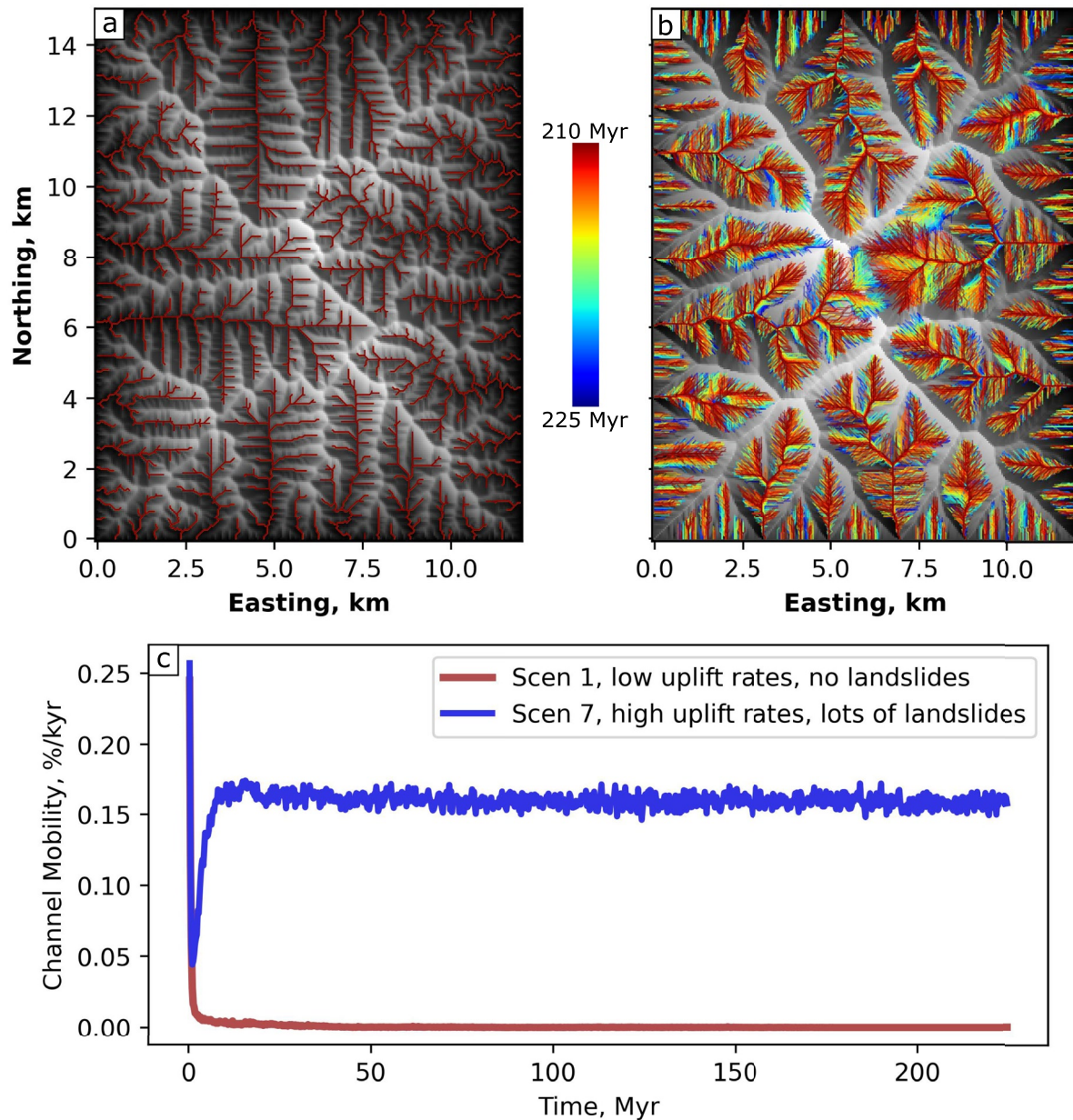
Figure 8. Mobility of the modeled fluvial network. (a and b) show the mobility of the fluvial channels between 210 and 225 Myr for the simulation with low uplift rates ((a) no landslides, scenario 1) versus high uplift rates ((b) frequent landsliding, scenario 7). River networks are colored through time with blue colors representing the river location at 210 Myr and red colors representing the river location at 225 Myr. When no landslides occur (a), fluvial mobility is minimal and previous river locations (blue) are overprinted by the most recent ones (red). (c) Channel mobility (% kyr^{-1}) through time. See Movie 3 for a dynamic representation.

the landscape approaches a fixed steady-state (Figure 8c). Active simulation of landslides (Figure 8b) results in a constantly changing drainage network in which the channel mobility hovers around 0.16% kyr^{-1} (Figure 8c).

6. Discussion

Bedrock landslides leave diagnostic signatures in topography (Figure 1 and Korup et al., 2004, 2007) that can be explained by a landscape evolution model that incorporates stochastic landsliding. Hillslope adjustment to rapid rock uplift results in elongated hillslopes, decreasing the extent of fluvial channels and the corresponding drainage density (Figure 3s) as predicted by threshold slope theory (Tucker & Bras, 1998). However, threshold slope models do not fully account for several characteristic features of landslide-dominated terrain

(Figure 1h). The stochastic model for bedrock landsliding studied here reproduces several of these features, including symmetrical slope distributions with patches of the landscape that exhibit slopes above the critical angle (Figure 1h). Modeled slopes having gradients steeper than the angle of repose can persist for durations set by the landslide-trigger recurrence interval (Figures 3n–3p). The stochastic model also produces quasi-planar slopes that bear signatures of incision by low-order channels (Figure 3d). In slope-area space, the intermittent interaction of fluvial incision and landsliding creates a region in which average slope only modestly changes with increasing drainage area (Figures 3k–3l). These patterns have been identified in a number field studies, which often interpret this region of slope-area space to represent colluvial channels (e.g., Booth et al., 2013; DiBiase et al., 2012, 2018; Montgomery & Foufoula-Georgiou, 1993; Tarolli & Dalla Fontana, 2009).

An implication of this model is that stochastic bedrock landslides cause persistent dynamism both on hillslopes and in channels. On hillslopes, the lack of an explicit limit on hillslope gradient allows slopes to oversteepen (i.e., to become steeper than the nominal stability limit). In fluvial channels, landslides episodically choke rivers with large quantities of sediment (Croissant et al., 2017). By running our simulations to a dynamic equilibrium we illustrate how landslides can cause channels to remain mobile through time in both a vertical and horizontal sense. Vertically, landslides trigger the formation of landslide dams that temporarily armor the bedrock and/or reroute the water to form epigenetic gorges. Both processes result in the formation of autogenic knickpoints (Figure 7), which results in an overall decrease of channel concavity when integrated over landscape evolution timescales (Figure 3q). Rapid valley aggradation due to landsliding and the formation of autogenic knickpoints is consistent with field observations (Korup, 2006; Ouimet et al., 2007; Yanites et al., 2010). This process ought to impact fluvial valley terrace stratigraphy in a autogenic manner, which would affect their value as recorders of allogenic controls. Both these implications underscore the importance of landsliding processes over geological timescales. Overall, episodic sediment supply hampers fluvial incision efficacy: an effect that would be further amplified if—as is often the case with bedrock landslides—landslide-derived material included boulders too large for the fluvial system to move (Glade et al., 2019; Shobe et al., 2016). The model runs also illustrate how episodic land-sliding can promote avulsion of upstream river channels and the valleys that contain them (Figure 8), even in the absence of other mechanisms for lateral erosion (e.g., Kwang et al., 2021; Langston & Tucker, 2018).

The HyLands model is able to account for commonly observed characteristics of mountainous terrain such as sediment concentration in valley networks, quasi-planar hillslopes etched with linear channel-like features, intermittent landslide dams, epigenetic gorges, and persistent migration of ridgelines and valleys. Yet, several processes were currently omitted from the model that could be investigated in future work. They include the simulation of grain-size-channel interactions (Egholm et al., 2013), stochastic storm events (Tucker & Bras, 2000), and more advanced landslide algorithms that can account for bedrock strength variability (Campforts, Vanacker, et al., 2020; Neely et al., 2019), complex rupture planes (Jeandet et al., 2019), shallow landslides (Claessens et al., 2007), and in-scar deposition. When landslide-fluvial interactions are explicitly treated, the model predicts that one consequence should be persistent dynamism (lateral migration) of ridgelines and valleys. Although the mechanism suggested by our experiments is not necessarily unique—a recent study that simulated lateral channel migration without landslides also showed persistent ridge and valley migration (Kwang et al., 2021)—our results add to a growing body of theory suggesting that such dynamism may be a common behavior in nature that emerges from channel-hillslope interactions.

7. Conclusion

Incorporating episodic landsliding into a landscape evolution model provides a mechanistic explanation for several diagnostic features of landslide-dominated topography. A simple stochastic treatment of landslide occurrence is both necessary and sufficient to account for patches of the landscape that exhibit slope angles well above the nominal stability threshold angle. The HyLands model reproduces steep, quasi-planar ridges decorated with closely spaced, shallowly incised channel-like features—a morphology that is also observed in mountainous, landslide-prone regions. The occurrence of landslides in terrain in which the erosion rate exceeds the maximum rate of soil production by weathering can explain the offset between measured soil production rates and catchment-wide denudation rates. Moreover, the activity of landslides integrated over geological times-cales accounts for the commonly observed situation in which landslide-derived sediment accumulates in fluvial reaches in steep landscapes. Finally, episodic landsliding accounts for persistent lateral mobility of channels, the valleys that contain them, and the ridgelines that surround them. Model results are consistent with inferences

from field observations that intermittent sediment burial of fluvial channels can trigger the formation of landslide dams and epigenetic gorges, which in turn can create autogenic knickpoints. Landslides are among the most effective geological processes shaping present-day terrain. Landscape evolution models that include landslides and associated sediment dynamics as an explicit set of processes reveal the topographic imprint of landslides over timescales relevant to the formation of mountain ranges. Landscape-scale understanding of interactions among landslides and the sediment cascades they trigger will ultimately help to improve our understanding of past and future environmental change on landscape dynamics.

Code Availability

The HyLands Landscape Evolution Model is built using the Landlab software package. The HyLands model builds on three new components: water and sediment is routed using the PriorityFloodFlowRouter, fluvial erosion and sediment transport is calculated using the SpaceLargeScaleEroder while bedrock landsliding and sediment runout is calculated using the BedrockLandslider. These and all other Landlab components used in this paper are part of the open source Landlab modeling framework, version 2.5.0 (Barnhart et al., 2020a; Hobley et al., 2017), which is part of the Community Surface Dynamics Modeling System (Tucker et al., 2021). Source code for the Landlab project is housed on GitHub: http://github.com/landlab/landlab (last access: 17 August 2022). Documentation, installation, instructions, and software dependencies for the entire Landlab project can be found at http://landlab.github.io/ (last access: 17 August 2022). A user manual with an accompanying Jupyter notebooks is available from https://github.com/BCampforts/hylands_modeling (last access: 17 August 2022). The Landlab project is tested on recent-generation Mac, Linux, and Windows platforms. The Landlab modeling framework is distributed under a MIT open-source license. The latest version of the Landlab software package, including the components developed for the HyLands model is archived at: https://doi.org/10.5281/zenodo.6951444 (last access: 17 August 2022).

Data Availability Statement

Digital elevation models used in this paper are derived from the LiDAR DEMs available through the topographical services of the state of Ohio. The Ohio DEMs can be downloaded directly from the following ZIP archive: http://gis3.oit.ohio.gov/ZIPARCHIVES/ELEVATION/LIDAR/Athens/ (last access: 17 August 2022). The Taiwan DEMs are available through: https://data.gov.tw/dataset/138563 (only available in Chinese, last access: 17 August 2022). Three movies illustrate the findings of this paper:

- Movie 1: illustrates the impact of landslides on shaping topography and sediment distribution under varying rock uplift rates and is available through figshare: https://doi.org/10.6084/m9.figshare.20503437.v1 (last access: 17 August 2022)
- Movie 2: illustrates the impact of landslides on the evolution of longitudinal river profiles and is available through figshare: https://doi.org/10.6084/m9.figshare.20505681.v1 (last access: 17 August 2022)
- Movie 3: illustrates the impact of landslides on stream channel migration in evolving landscapes and is available through figshare: https://doi.org/10.6084/m9.figshare.20505693.v1 (last access: 17 August 2022).

References

Andrews, D., & Bucknam, R. C. (1987). Fitting degradation of shoreline scarps by a nonlinear diffusion model. *Journal of Geophysical Research*, *92*(B12), 12857–12867. https://doi.org/10.1029/jb092ib12p12857

Barnes, R., Lehman, C., & Mulla, D. (2014). Priority-flood: An optimal depression-filling and watershed-labeling algorithm for digital elevation models. *Computers & Geosciences*, *62*, 117–127. Retrieved from https://doi.org/10.1016/j.cageo.2013.04.024

Barnhart, K. R., Glade, R. C., Shobe, C. M., & Tucker, G. E. (2019). Terrainbento 1.0: A Python package for multi-model analysis in long-term drainage basin evolution. *Geoscientific Model Development Discussions*, *12*(4), 1267–1297. https://doi.org/10.5194/gmd-12-1267-2019

Barnhart, K. R., Hutton, E. W. H., Tucker, G. E., Gasparini, N. M., Istanbulluoglu, E., Hobley, D. E. J., et al. (2020a). Short communication: Landlab v2.0: A software package for Earth surface dynamics. *Earth Surface Dynamics*, *8*(2), 379–397. https://doi.org/10.5194/esurf-8-379-2020

Barnhart, K. R., Hutton, E. W. H., Tucker, G. E., Gasparini, N. M., Istanbulluoglu, E., Hobley, D. E. J., et al. (2020b). Short communication: Landlab v2.0: A software package for Earth surface dynamics. *Earth Surface Dynamics*, *8*(2), 379–397. https://doi.org/10.5194/esurf-8-379-2020

Beeson, H. W., McCoy, S. W., & Keen-Zebert, A. (2017). Geometric disequilibrium of river basins produces long-lived transient landscapes. *Earth and Planetary Science Letters*, *475*, 34–43. https://doi.org/10.1016/j.epsl.2017.07.010

Booth, A. M., Roering, J. J., & Rempel, A. W. (2013). Topographic signatures and a general transport law for deep-seated landslides in a landscape evolution model. *Journal of Geophysical Research: Earth Surface*, *118*(2), 603–624. https://doi.org/10.1002/jgrf.20051

Broeckx, J., Rossi, M., Lijnen, K., Campforts, B., Poesen, J., & Vanmaercke, M. (2020). Landslide mobilization rates: A global analysis and model. *Earth-Science Reviews*, *201*, 102972. https://doi.org/10.1016/j.earscirev.2019.102972

Burbank, D. W., Leland, J., Fielding, E., Anderson, R. S., Brozovic, N., Reid, M. R., & Duncan, C. (1996). Bedrock incision, rock uplift and threshold hillslopes in the Northwestern Himalayas. *Nature*, *379*(6565), 505–510. https://doi.org/10.1038/379505a0

Campforts, B., Schwanghart, W., & Govers, G. (2017). Accurate simulation of transient landscape evolution by eliminating numerical diffusion: The TTLEM 1.0 model. *Earth Surface Dynamics*, *5*(1), 47–66. https://doi.org/10.5194/esurf-5-47-2017

Campforts, B., Shobe, C. M., Steer, P., Vanmaercke, M., Lague, D., & Braun, J. (2020). HyLands 1.0: A hybrid landscape evolution model to simulate the impact of landslides and landslide-derived sediment on landscape evolution. *Geoscientific Model Development*, *13*(9), 3863–3886. https://doi.org/10.5194/gmd-13-3863-2020

Campforts, B., Vanacker, V., Herman, F., Vanmaercke, M., Schwanghart, W., Tenorio, G. E., et al. (2020). Parameterization of river incision models requires accounting for environmental heterogeneity: Insights from the tropical Andes. *Earth Surface Dynamics*, *8*(2), 447–470. https://doi.org/10.5194/esurf-8-447-2020

Carretier, S., Martinod, P., Reich, M., & Godderis, Y. (2016). Modelling sediment clasts transport during landscape evolution. *Earth Surface Dynamics*, *4*(1), 237–251. https://doi.org/10.5194/esurf-4-237-2016

Carson, M. A., & Petley, D. J. (1970). The existence of threshold hillslopes in the denudation of the landscape. *Transactions of the Institute of British Geographers*, *49*(49), 71. https://doi.org/10.2307/621642

Champel, B. (2002). Growth and lateral propagation of fault-related folds in the Siwaliks of Western Nepal: Rates, mechanisms, and geomorphic signature. *Journal of Geophysical Research*, *107*(B6), 2111. https://doi.org/10.1029/2001JB000578

Claessens, L., Schoorl, J., & Veldkamp, A. (2007). Modelling the location of shallow landslides and their effects on landscape dynamics in large watersheds: An application for Northern New Zealand. *Geomorphology*, *87*(1–2), 16–27. https://doi.org/10.1016/j.geomorph.2006.06.039

Clubb, F. J., Mudd, S. M., Milodowski, D. T., Hurst, M. D., & Slater, L. J. (2014). Objective extraction of channel heads from high-resolution topographic data. *Water Resources Research*, *50*(5), 4283–4304. https://doi.org/10.1002/2013WR015167

Croissant, T., Lague, D., Steer, P., & Davy, P. (2017). Rapid post-seismic landslide evacuation boosted by dynamic river width. *Nature Geoscience*, *10*(9), 680–684. https://doi.org/10.1038/ngeo3005

Crovelli, R. A. (2000). Probability models for estimation of number and costs of landslides (Vol. Open-File; Technical Report). https://doi.org/10.3133/ofr00249

Culmann, K. (1875). *Die Graphische Statike*. Verlag von Meyer and Zeller. Retrieved from https://archive.org/details/diegraphischest01culmgoog/page/n8/mode/2up

Dahlquist, M. P., West, A. J., & Li, G. (2018). Landslide-driven drainage divide migration. *Geology*, *46*(5), 403–406. https://doi.org/10.1130/G39916.1

Davy, P., & Lague, D. (2009). Fluvial erosion/transport equation of landscape evolution models revisited. *Journal of Geophysical Research*, *114*(3), 1–16. https://doi.org/10.1029/2008JF001146

DeLisle, C., Yanites, B. J., Chen, C.-Y., Shyu, J. B. H., & Rittenour, T. M. (2022). Extreme event-driven sediment aggradation and erosional buffering along a tectonic gradient in southern Taiwan. *Geology*, *50*(1), 16–20. https://doi.org/10.1130/G49304.1

Demoulin, A. (1998). Testing the tectonic significance of some parameters of longitudinal river profiles: The case of the Ardenne (Belgium, NW Europe). *Geomorphology*, *24*(2–3), 189–208. https://doi.org/10.1016/S0169-555X(98)00016-6

Densmore, A. L., Ellis, M. A., & Anderson, R. S. (1998). Landsliding and the evolution of normal-fault-bounded mountains. *Journal of Geophysical Research*, *103*(B7), 15203–15219. https://doi.org/10.1029/98jb00510

Depicker, A., Govers, G., Jacobs, L., Campforts, B., Uwihirwe, J., & Dewitte, O. (2021). Interactions between deforestation, landscape rejuvenation, and shallow landslides in the North Tanganyika–Kivu rift region, Africa. *Earth Surface Dynamics*, *9*(3), 445–462. https://doi.org/10.5194/esurf-9-445-2021

DiBiase, R. A., Heimsath, A. M., & Whipple, K. X. (2012). Hillslope response to tectonic forcing in threshold landscapes. *Earth Surface Processes and Landforms*, *37*(8), 855–865. https://doi.org/10.1002/esp.3205

DiBiase, R. A., Rossi, M. W., & Neely, A. B. (2018). Fracture density and grain size controls on the relief structure of bedrock landscapes. *Geology*, *46*(5), 399–402. https://doi.org/10.1130/g40006.1

DiBiase, R. A., Whipple, K. X., Heimsath, A. M., & Ouimet, W. B. (2010). Landscape form and millennial erosion rates in the San Gabriel Mountains, CA. *Earth and Planetary Science Letters*, *289*(1–2), 134–144. https://doi.org/10.1016/j.epsl.2009.10.036

Dietrich, W. E., Bellugi, D. G., Sklar, L. S., Stock, J. D., Heimsath, A. M., & Roering, J. J. (2003). Geomorphic transport laws for predicting landscape form and dynamics. *Geophysical Monograph Series*, *135*, 103–132. https://doi.org/10.1029/135GM09

Dixon, J. L., & von Blanckenburg, F. (2012). Soils as pacemakers and limiters of global silicate weathering. *Comptes Rendus Geoscience*, *344*(11–12), 597–609. https://doi.org/10.1016/j.crte.2012.10.012

Egholm, D. L., Knudsen, M. F., & Sandiford, M. (2013). Lifespan of mountain ranges scaled by feedbacks between landsliding and erosion by rivers. *Nature*, *498*(7455), 475–478. https://doi.org/10.1038/nature12218

Eisbacher, & Clague (1984). Destructive mass movements in high mountains: Hazard and management (Paper/Geological Survey of Canada). *Geological Survey of Canada offices*.

Fan, X., Scaringi, G., Korup, O., West, A. J., van Westen, C. J., Tanyas, H., et al. (2019). Earthquake-induced chains of geologic hazards: Patterns, mechanisms, and impacts. *Reviews of Geophysics*, *57*(2), 421–503. https://doi.org/10.1029/2018RG000626

Fisher, S. P., Fanaff, A. S., & Picking, L. W. (1968). Landslides of Southeastern Ohio. *The Ohio Journal of Science*, *68*(2), 65–80. Retrieved from https://linkinghub.elsevier.com/retrieve/pii/0378112796037723http://hdl.handle.net/1811/5367

Fuller, C., Willett, S., & Fisher, D., & Lu, C. (2006). A thermomechanical wedge model of Taiwan constrained by fission-track thermochronometry. *Tectonophysics*, *425*(1), 1–24. https://doi.org/10.1016/j.tecto.2006.05.018

Ganti, V., Passalacqua, P., & Foufoula-Georgiou, E. (2012). A sub-grid scale closure for nonlinear hillslope sediment transport models. *Journal of Geophysical Research*, *117*(F2). https://doi.org/10.1029/2011jf002181

George, D. L., & Iverson, R. M. (2014). A depth-averaged debris-flow model that includes the effects of evolving dilatancy. II. Numerical predictions and experimental tests. *Proceedings of the Royal Society A: Mathematical, Physical & Engineering Sciences*, *470*(2170), 20130820. https://doi.org/10.1098/rspa.2013.0820

Glade, R. C., Shobe, C. M., Anderson, R. S., & Tucker, G. E. (2019). Canyon shape and erosion dynamics governed by channel-hillslope feedbacks. *Geology*, *47*(7), 650–654. https://doi.org/10.1130/g46219.1

Goebel, P. C., Hix, D. M., & Jones, J. W. (1996). Development of mixed-oak forests in southeastern Ohio: A comparison of second-growth and old-growth forests. *Forest Ecology and Management*, *84*(1–3), 1–21. https://doi.org/10.1016/0378-1127(96)03772-3

Harel, M.-A., Mudd, S., & Attal, M. (2016). Global analysis of the stream power law parameters based on worldwide ^{10}Be denudation rates. *Geomorphology*, *268*, 184–196. https://doi.org/10.1016/j.geomorph.2016.05.035

Hasbargen, L. E., & Paola, C. (2000). Landscape instability in an experimental drainage basin. *Geology*, *28*(12), 1067. https://doi.org/10.1130/0091-7613(2000)28<1067:liiaed>2.0.co;2

Heimsath, A., DiBiase, R., & Whipple, K. (2012). Soil production limits and the transition to bedrock-dominated landscapes. *Nature Geoscience*, *5*(3), 210–214. https://doi.org/10.1038/ngeo1380

Heimsath, A. M., Dietrichs, W. E., Nishiizuml, K., & Finkel, R. C. (1997). The soil production function and landscape equilibrium. *Nature*, *388*(6640), 358–361. https://doi.org/10.1038/41056

Hobley, D. E., Adams, J. M., Nudurupati, S. S., Hutton, E. W., Gasparini, N. M., Istanbulluoglu, E., & Tucker, G. E. (2017). Creative computing with Landlab: An open-source toolkit for building, coupling, and exploring two-dimensional numerical models of Earth-surface dynamics. *Earth Surface Dynamics*, *5*(1), 21–46. https://doi.org/10.5194/esurf-5-21-2017

Hovius, N., Stark, C. P., & Allen, P. A. (1997). Sediment flux from a mountain belt derived by landslide mapping. *Geology*, *25*(3), 231–234. https://doi.org/10.1130/0091-7613(1997)025<0231:sffamb>2.3.co;2

Hovius, N., Stark, C. P., Hao-Tsu, C., Jiun-Chuan, L., Hao-Tsu, C., & Jiun-Chuan, L. (2000). Supply and removal of sediment in a landslide-dominated mountain belt: Central Range, Taiwan. *The Journal of Geology*, *108*(1), 73–89. https://doi.org/10.1086/314387

Iverson, R. M., & George, D. L. (2014). A depth-averaged debris-flow model that includes the effects of evolving dilatancy. I. Physical basis. *Proceedings of the Royal Society A: Mathematical, Physical & Engineering Sciences*, *470*(2170), 20130819. https://doi.org/10.1098/rspa.2013.0819

Jeandet, L., Steer, P., Lague, D., & Davy, P. (2019). Coulomb mechanics and relief constraints explain landslide size distribution. *Geophysical Research Letters*, *46*(8), 4258–4266. https://doi.org/10.1029/2019GL082351

Johnstone, S. A., & Hilley, G. E. (2015). Lithologic control on the form of soil-mantled hillslopes. *Geology*, *43*(1), 83–86. https://doi.org/10.1130/G36052.1

Korup, O. (2006). Effects of large deep-seated landslides on hillslope morphology, Western Southern Alps, New Zealand. *Journal of Geophysical Research*, *111*(F1), F01018. https://doi.org/10.1029/2004JF000242

Korup, O. (2008). Rock type leaves topographic signature in landslide-dominated mountain ranges. *Geophysical Research Letters*, *35*(11), L11402. https://doi.org/10.1029/2008GL034157

Korup, O., Clague, J. J., Hermanns, R. L., Hewitt, K., Strom, A. L., & Weidinger, J. T. (2007). Giant landslides, topography, and erosion. *Earth and Planetary Science Letters*, *261*(3–4), 578–589. https://doi.org/10.1016/j.epsl.2007.07.025

Korup, O., McSaveney, M. J., & Davies, T. R. (2004). Sediment generation and delivery from large historic landslides in the Southern Alps, New Zealand. *Geomorphology*, *61*(1–2), 189–207. https://doi.org/10.1016/j.geomorph.2004.01.001

Kwang, J. S., Langston, A. L., & Parker, G. (2021). The role of lateral erosion in the evolution of nondendritic drainage networks to dendricity and the persistence of dynamic networks. *Proceedings of the National Academy of Sciences*, *118*(16), e2015770118. https://doi.org/10.1073/pnas.2015770118

Langston, A. L., & Tucker, G. E. (2018). Developing and exploring a theory for the lateral erosion of bedrock channels for use in landscape evolution models. *Earth Surface Dynamics*, *6*(1), 1–27. https://doi.org/10.5194/esurf-6-1-2018

Larsen, I. J., Almond, P. C., Eger, A., Stone, J. O., Montgomery, D. R., & Malcolm, B. (2014). Rapid soil production and weathering in the southern Alps, New Zealand. *Science*, *343*(6171), 637–640. https://doi.org/10.1126/science.1244908

Larsen, I. J., & Montgomery, D. R. (2012). Landslide erosion coupled to tectonics and river incision. *Nature Geoscience*, *5*(7), 468–473. https://doi.org/10.1038/ngeo1479

Lupker, M., Blard, P., Lavé, J., France-Lanord, C., Leanni, L., Puchol, N., et al. (2012). ¹⁰Be-derived Himalayan denudation rates and sediment budgets in the Ganga basin. *Earth and Planetary Science Letters*, *333*, 146–156. https://doi.org/10.1016/j.epsl.2012.04.020

Montgomery, D. R. (2001). Slope distributions, threshold hillslopes, and steady-state topography. *American Journal of Science*, *301*(4–5), 432–454. https://doi.org/10.2475/ajs.301.4-5.432

Montgomery, D. R., & Dietrich, W. E. (1994). A physically based model for the topographic control on shallow landsliding. *Water Resources Research*, *30*(4), 1153–1171. https://doi.org/10.1029/93WR02979

Montgomery, D. R., & Foufoula-Georgiou, E. (1993). Channel network source representation using digital elevation models. *Water Resources Research*, *29*(12), 3925–3934. https://doi.org/10.1029/93WR02463

Neely, A. B., DiBiase, R. A., Corbett, L. B., Bierman, P. R., & Caffee, M. W. (2019). Bedrock fracture density controls on hillslope erodibility in steep, rocky landscapes with patchy soil cover, southern California, USA. *Earth and Planetary Science Letters*, *522*, 186–197. https://doi.org/10.1016/j.epsl.2019.06.011

Ouimet, W. B., Whipple, K. X., Crosby, B. T., Johnson, J. P., & Schildgen, T. F. (2008). Epigenetic gorges in fluvial landscapes. *Earth Surface Processes and Landforms*, *33*(13), 1993–2009. https://doi.org/10.1002/esp.1650

Ouimet, W. B., Whipple, K. X., Royden, L. H., Sun, Z., & Chen, Z. (2007). The influence of large landslides on river incision in a transient landscape: Eastern margin of the Tibetan Plateau (Sichuan, China). *Bulletin of the Geological Society of America*, *119*(11–12), 1462–1476. https://doi.org/10.1130/B26136.1

Pelletier, J. D. (2004). Persistent drainage migration in a numerical landscape evolution model. *Geophysical Research Letters*, *31*(20), 4–7. https://doi.org/10.1029/2004GL020802

Portenga, E., & Bierman, P. (2011). Understanding Earth's eroding surface with ¹⁰Be. *Geological Society of America Today*, *21*(8), 4–10. https://doi.org/10.1130/g111a.1

Pourghasemi, H. R., Teimoori Yansari, Z., Panagos, P., & Pradhan, B. (2018). Analysis and evaluation of landslide susceptibility: A review on articles published during 2005–2016 (periods of 2005–2012 and 2013–2016). *Arabian Journal of Geosciences*, *11*(9), 193. https://doi.org/10.1007/s12517-018-3531-5

Roering, J. J., Kirchner, J. W., & Dietrich, W. E. (1999). Evidence for nonlinear, diffusive sediment transport on hillslopes and implications for landscape morphology. *Water Resources Research*, *35*(3), 853–870. https://doi.org/10.1029/1998WR900090

Roering, J. J., Mackey, B. H., Handwerger, A. L., Booth, A. M., Schmidt, D. A., Bennett, G. L., & Cerovski-Darriau, C. (2015). Beyond the angle of repose: A review and synthesis of landslide processes in response to rapid uplift, Eel River, Northern California. *Geomorphology*, *236*, 109–131. https://doi.org/10.1016/j.geomorph.2015.02.013

Schmidt, K. M., & Montgomery, D. R. (1995). Limits to relief. *Science*, *270*(5236), 617–620. https://doi.org/10.1126/science.270.5236.617

Selby, M. J. (1982). Controls on the stability and inclinations of hillslopes formed on hard rock. *Earth Surface Processes and Landforms*, *7*(5), 449–467. https://doi.org/10.1002/esp.3290070506

Shobe, C. M., Tucker, G. E., & Anderson, R. S. (2016). Hillslope-derived blocks retard river incision. *Geophysical Research Letters*, *43*(10), 5070–5078. https://doi.org/10.1002/2016GL069262

Shobe, C. M., Tucker, G. E., & Barnhart, K. R. (2017). The SPACE 1.0 model: A Landlab component for 2-D calculation of sediment transport, bedrock erosion, and landscape evolution. *Geoscientific Model Development*, *10*(12), 4577–4604. https://doi.org/10.5194/gmd-10-4577-2017

Tarolli, P., & Dalla Fontana, G. (2009). Hillslope-to-valley transition morphology: New opportunities from high resolution DTMs. *Geomorphology*, *113*(1–2), 47–56. Retrieved from https://doi.org/10.1016/j.geomorph.2009.02.006

Tucker, G. E., & Bras, R. L. (1998). Hillslope processes, drainage density, and landscape morphology. *Water Resources Research*, *34*(10), 2751–2764. https://doi.org/10.1029/98WR01474

Tucker, G. E., & Bras, R. L. (2000). A stochastic approach to modeling the role of rainfall variability in drainage basin evolution. *Water Resources Research*, *36*(7), 1953–1964. https://doi.org/10.1029/2000WR900065

Tucker, G. E., Catani, F., Rinaldo, A., & Bras, R. L. (2001). Statistical analysis of drainage density from digital terrain data. *Geomorphology*, *36*(3–4), 187–202. https://doi.org/10.1016/S0169-555X(00)00056-8

Tucker, G. E., & Hancock, G. R. (2010). Modelling landscape evolution. *Earth Surface Processes and Landforms*, *35*(1), 28–50. https://doi.org/10.1002/esp.1952

Tucker, G. E., Hutton, E., Piper, M., Campforts, B., Gan, T., Barnhart, K., et al. (2021). CSDMS: A community platform for numerical modeling of Earth-surface processes. *Geoscientific Model Development Discussions*, *15*, 1–40. https://doi.org/10.5194/gmd-2021-223

Tucker, G. E., & Whipple, K. X. (2002). Topographic outcomes predicted by stream erosion models: Sensitivity analysis and intermodel comparison. *Journal of Geophysical Research*, *107*(B9), 2179. https://doi.org/10.1029/2001JB000162

Whipple, K. X. (2001). Fluvial landscape response time: How plausible is steady-state denudation? *American Journal of Science*, *301*(4–5), 313–325. https://doi.org/10.2475/ajs.301.4-5.313

Wobus, C., Whipple, K. X., Kirby, E., Snyder, N., Johnson, J., Spyropolou, K., et al. (2006). Tectonics from topography: Procedures, promise, and pitfalls. In S. D. Willett, N. Hovius, M. T. Brandon, & D. M. Fisher (Eds.), *Special paper of the Geological Society of America* (Vol. 398, pp. 55–74). Geological Society of America. https://doi.org/10.1130/2006.2398(04)

Yanites, B. J., Tucker, G. E., Mueller, K. J., & Chen, Y.-G. G. (2010). How rivers react to large earthquakes: Evidence from central Taiwan. *Geology*, *38*(7), 639–642. https://doi.org/10.1130/G30883.1

Zaprowski, B. J., Pazzaglia, F. J., & Evenson, E. B. (2005). Climatic influences on profile concavity and river incision. *Journal of Geophysical Research*, *110*(3), F03004. https://doi.org/10.1029/2004JF000138